REPORT

Glacial lake outburst floods as drivers of fluvial erosion in the Himalaya

Kristen L. Cook[1]*, Christoff Andermann[1], Florent Gimbert[1,2], Basanta Raj Adhikari[3], Niels Hovius[1,4]

Himalayan rivers are frequently hit by catastrophic floods that are caused by the failure of glacial lake and landslide dams; however, the dynamics and long-term impacts of such floods remain poorly understood. We present a comprehensive set of observations that capture the July 2016 glacial lake outburst flood (GLOF) in the Bhotekoshi/Sunkoshi River of Nepal. Seismic records of the flood provide new insights into GLOF mechanics and their ability to mobilize large boulders that otherwise prevent channel erosion. Because of this boulder mobilization, GLOF impacts far exceed those of the annual summer monsoon, and GLOFs may dominate fluvial erosion and channel-hillslope coupling many tens of kilometers downstream of glaciated areas. Long-term valley evolution in these regions may therefore be driven by GLOF frequency and magnitude, rather than by precipitation.

Lake outburst floods (LOFs) have long been recognized as both a hazard and major agent of geomorphic change in the Himalaya (1–5). These floods originate from lakes that have formed behind a landslide dam or in association with a glacier, dammed by a frontal moraine or glacial ice. Such lakes can drain catastrophically for several reasons, including mass movements or avalanches into the lake, seismic activity, piping within the dam, overtopping of the dam, or degradation of blocking ice (4, 6). The resulting floods can have short-lived discharges up to several orders of magnitude higher than background discharges in the receiving rivers (7). Because of their magnitude and unpredictability, LOFs can be highly destructive and compromise local infrastructure such as roads, buildings, and hydropower facilities (3, 8–10).

Although large LOFs have been recognized as strongly affecting river morphology and dynamics (4, 11–13), they are often treated as one-off events. The potential impact of repeated LOFs, particularly the less dramatic small-to-medium magnitude floods, on the longer-term behavior of the fluvial system has received little attention. The impact of individual LOF events must be considered along with LOF frequency and measured against the accumulated effect of annual monsoon floods of variable size. We evaluate the importance of glacial lake outburst floods (GLOFs) in driving fluvial erosion by examining the Bhotekoshi/Sunkoshi River, where we compare monsoon floods to a GLOF that occurred in July 2016. In addition to documenting relative impacts and discharges, we use seismic observations to gain insight into GLOF dynamics, and we explore the role of boulder-sized sediment in promoting GLOF-driven erosion.

On the night of 5 July 2016, Gongbatongshacuo Lake, a 1.7×10^4-m² moraine-dammed lake in the Tibet Autonomous Region, China, drained catastrophically, releasing approximately 1.1×10^5 m³ of water (14). The cause of the breach is unknown, but fresh deposits above the lake suggest that it may have been associated with a debris flow event, possibly increasing the volume of the flood (Fig. 1B). The flood proceeded down the Zhangzangbo River into the Poiqu/Bhotekoshi/Sunkoshi River and caused severe damage in the Bhotekoshi valley, destroying the intake dam of a hydropower project, the Araniko highway, and numerous buildings in the towns of Kodari and Tatopani. The zone of damage sits within the area affected by strong ground motion and landsliding induced by the 2015 moment magnitude 7.8 Gorkha earthquake, which had an estimated return time of a few hundred years (15, 16).

The 2016 GLOF passed through an array of six broadband seismometers installed in 2015 along the Bhotekoshi River valley, 28 to 35 km downstream of the Zhangzangbo confluence (Fig. 1). Because both turbulent flow (17) and bedload transport (18) in rivers can generate detectable seismic ground motion (19), the seismic record of the GLOF can be used to probe the flood and sediment dynamics at high temporal and spatial resolution. The seismic records for each near-river station contain two distinct pulses of high-amplitude noise (Fig. 1C). The first is the flood front, which propagates between stations at 8.7 m/s. The abrupt rise of seismic power at each station suggests that the maximum flow depth was reached within 2 min. At Chaku station, this corresponded to a calculated maximum discharge of 1500 to 2100 m³/s (Fig. 2 and table S1). The second pulse is of higher magnitude but travels slower, at 5 m/s. The total duration of the flood, including both pulses, at each of the stations was less than an hour. We interpret the first pulse as a water wave and the second as a package of coarse sediment, on the basis of the following reasoning: If both pulses were associated with propagating water waves, then the more energetic second wave should have a greater flow depth and travel faster (17). The prediction from theory is that near-river stations should be especially sensitive to coarse sediment, whereas far-river stations should be predominantly sensitive to water flow (17, 18) (fig. S1). The second wave was prominent at near-river stations but much weaker at farther seismic stations, consistent with the theory (fig. S2). Theory also predicts that coarse-sediment transport generates seismic noise at higher frequencies compared to turbulent flow (17, 18) (fig. S1), and power spectra from the two pulses indicate an increase in power at higher frequencies during the second pulse (fig. S3).

The ratio of the pulse velocities is 0.6, matching bedload/water velocity ratios observed experimentally and in small-river settings (20). This velocity difference ensured that the flood front outpaced any entrained sediment and therefore remained depleted in bedload.

Field- and satellite-based observations show that the GLOF affected the river channel over a ~40-km stretch between the confluence with the Zhangzangbo River and Barabise town (Fig. 1). The flood impact extended into the adjacent hillslopes through undercutting and destabilization of the river banks, leading to bank collapses, slumps, and landslides. The extensive flood-induced damage to local infrastructure was almost exclusively the result of bank erosion and mass wasting, rather than inundation (fig. S4).

We quantified the magnitude of channel, bank, and hillslope change with repeat terrestrial lidar surveys from October 2015, March 2016, and November 2016 in nine locations that together covered 20% of the channel length between Khukundol and Barabise (Fig. 1 and table S2). Eight of the scanned reaches experienced downcutting varying from 1 to 10 m, whereas one had no bed-elevation change (Fig. 3).

We observed bank erosion in numerous sections of the channel, and all scanned reaches contained segments with at least 2 m of lateral erosion (Fig. 3 and fig. S5). Bank erosion included parallel retreat of steep banks and erosion and undercutting at the base of slopes. Analysis of 5-m-resolution RapidEye imagery (table S3) indicates that the 2016 GLOF caused the mean width of the active channel between the Zhangzangbo confluence and Barabise to increase from 29.5 ± 3 m

[1]GFZ German Research Centre for Geosciences, Potsdam, Germany. [2]University of Grenoble Alpes, CNRS, IRD, Institut des Géosciences de l'Environnement (IGE), Grenoble, France. [3]Department of Civil Engineering, Pulchowk Campus, Institute of Engineering, Tribhuvan University, Nepal. [4]Institute of Earth and Environmental Science, Potsdam University, Potsdam, Germany.
*Corresponding author. Email: klcook@gfz-potsdam.de
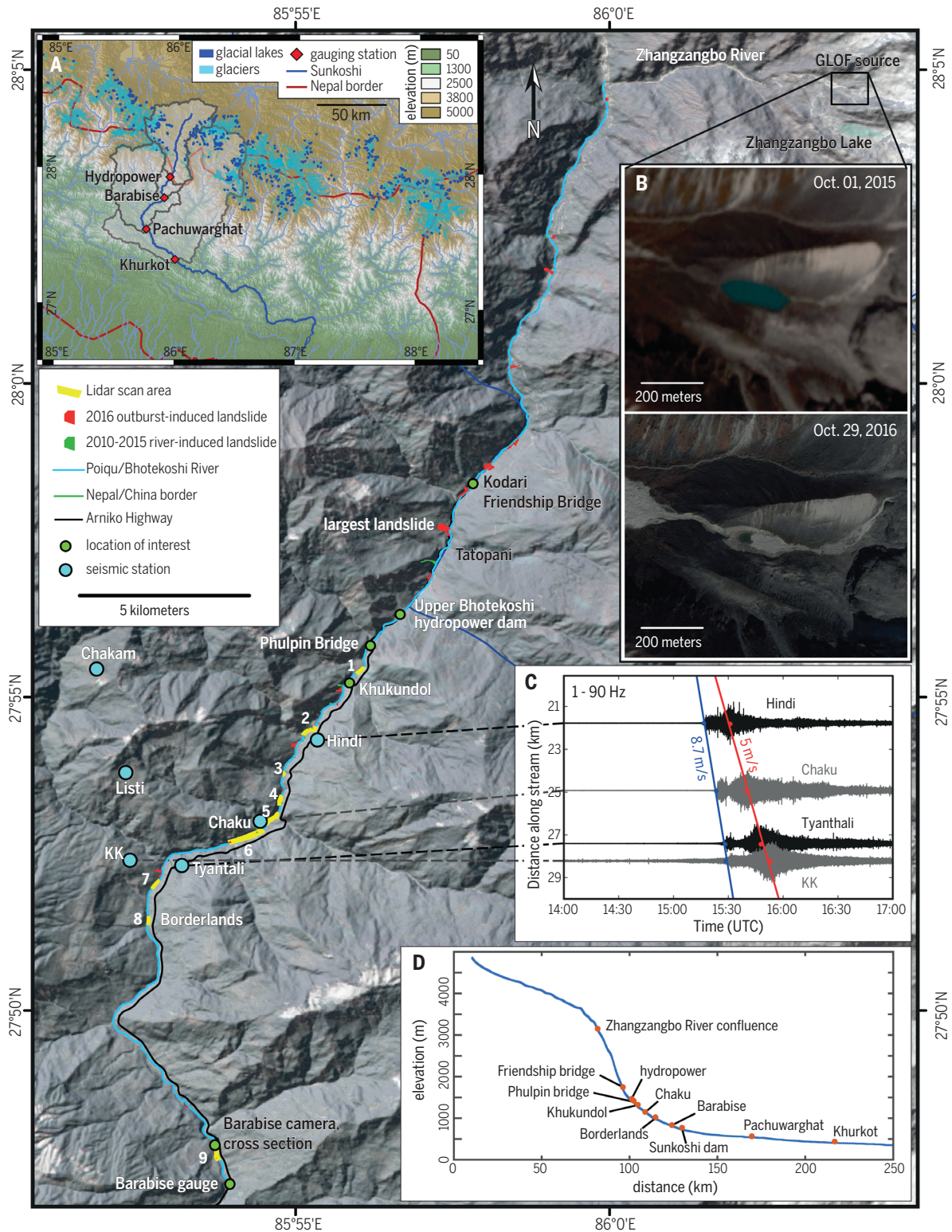
Fig. 1. Map of the Bhotekoshi study region. Scanned reaches, mapped landslides, seismic stations, and locations discussed in the text are shown. White numbers 1 to 9 indicate each scan location, with reference to table S1. (**A**) The inset provides the regional context, with glaciers and glacial lakes shown (9). The shading and black outlines indicate drainage basins upstream of Khurkot, Pachuwarghat, Barabise, and the Upper Bhotekoshi hydropower dam. (**B**) Google Earth and RapidEYE imagery showing a magnified view of the lake that was the source of the outburst flood, both before the bursting event in October 2015 (top) and after in October 2016 (bottom). (**C**) Seismic record of GLOF propagation. Normalized ground velocity time series from four stations at different distances downstream of the Zhangzangbo confluence. Dots indicate the manually picked pulse arrivals. Straight lines correspond to linear fits of distance versus time and yield the pulse velocities. UTC, universal time coordinated. (**D**) Longitudinal profile from the Advanced Land Observing Satellite 12.5-m digital elevation model of the Poiqu/Bhotekoshi/Sunkoshi River, with locations of interest marked.

in 2015 to 41.3 ± 3 m in 2016, with highly variable widening throughout the mapped area (Fig. 3). The lateral changes in 2016 contrast with the stability of the river between 2010 and 2015. During these six monsoon seasons, changes to the river channel were minimal and were associated with external influences such as anthropogenic modification, local landsliding, and tributary input. Despite the large amount of landslide debris produced during the 2015 Gorkha earthquake (15, 16), the channel underwent minimal modification during the 2015 monsoon (Fig. 3 and fig. S6).

Lateral erosion of the channel by the GLOF led to the activation of landslides that propagated
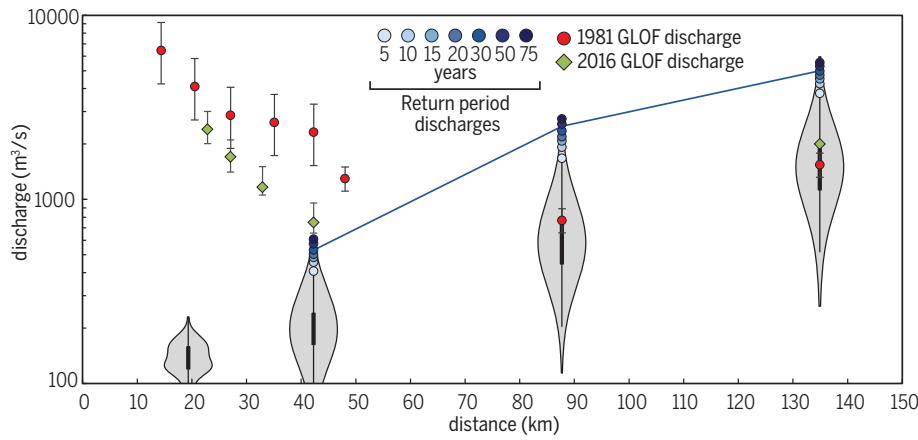
Fig. 2. Discharge with distance downstream of the Zhangzangbo confluence. Data from table S4. Estimated discharges for the 1981 (11) and 2016 GLOFs and the calculated discharges for floods of varying return periods (5 to 75 years). The blue line connects the 30-year-return discharges. The violin plots show the full distribution of monsoon discharges (July and August) for each hydrological station (hydropower dam, Barabise, Pachuwarghat, and Khurkot). Error bars indicate estimated uncertainty (for details, see materials and methods).
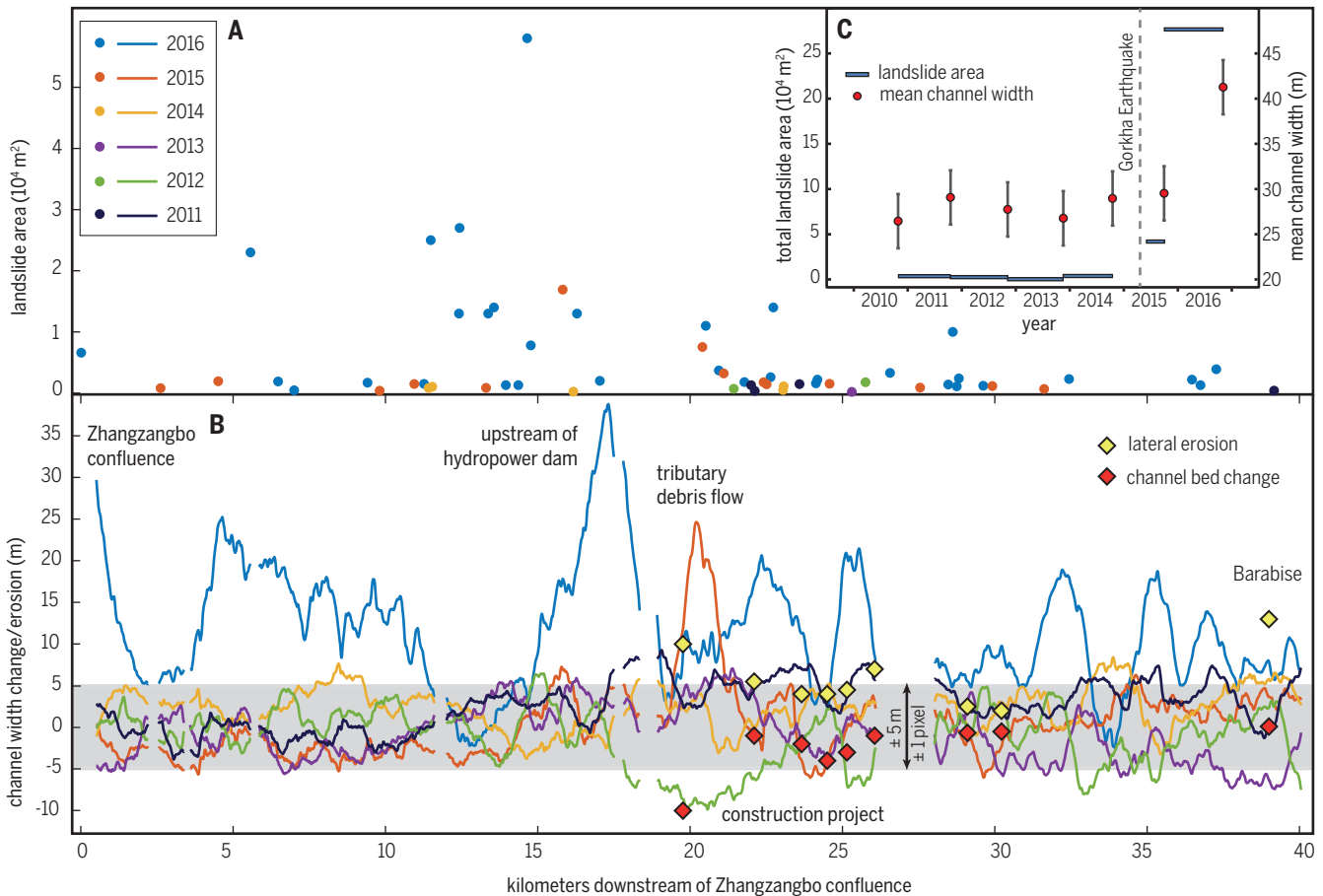
Fig. 3. Summary of monsoon- and GLOF-driven changes in the Poiqu/Bhotekoshi channel. (**A**) Landslide areas with distance downstream of the Zhangzangbo confluence from 2010 to 2016; each point represents one landslide. (**B**) Width changes from 2010 to 2016 and lidar-derived GLOF changes. The gray bar indicates an uncertainty of ±5 m, equivalent to ±1 pixel in the satellite imagery. Data have been smoothed by applying a running average over a 1-km window. Diamonds show the maximum values of lateral erosion and channel-bed elevation change from each of the lidar-scanned reaches. The lidar-derived lateral erosion values are not expected to match the satellite-derived width changes because the satellite-derived data have been smoothed. (**C**) Time series summary of data from (A) and (B). The mean channel widths through time and areas of river-related landslides that occurred during each monsoon season are shown.

up the hillslopes (Fig. 1). Mapping from RapidEye imagery shows that 26 landslides in which the zone of failure is connected to the channel formed during the 2016 monsoon. The cumulative area of these landslides was ~100 times larger than the landslide area during a typical year (2009 to 2014) and five times larger than that during the 2015 monsoon, which solicited an unusually high rate of landsliding after the Gorkha earthquake (Figs. 1 and 3).

The 2016 GLOF had an impact on the river and adjacent hillslopes that far outstripped that of the monsoon floods of 2009 to 2016. The effects of the 2016 GLOF are similar to the documented effects of a previous GLOF on the Poiqu/Bhotekoshi/Sunkoshi River on 11 July 1981. This flood contained an estimated 1.9×10^7 m^3 of water released from the Zhangzangbo Lake, near the source of the 2016 flood (11) (Fig. 1). The damage from the 1981 flood mirrors that from the 2016 flood and included the destruction of a hydropower dam, sections of the Araniko highway, and several bridges. Numerous landslides related to this outburst flood occurred along the Bhotekoshi River (11).

We attribute the large discrepancy between the impacts of the GLOFs and the monsoon floods to the ubiquity of extremely coarse landslide-derived boulders (>1 m in diameter) in the bed and banks of the Bhotekoshi River (fig. S7). River-channel stability during floods is related to the stability of boulder-sized clasts that define the channel geometry (21, 22). Although the threshold discharge for mobilizing these boulders varies with clast location and size, the threshold generally does not appear to be exceeded during the monsoon. On the basis of field observations and Google Earth imagery, movement of large boulders has not taken place during monsoon floods since at least 2004 (fig. S8). The smallest boulders we can reliably identify as stable in Google Earth imagery are about 2 to 3 m in diameter, smaller than boulders that moved in these reaches during the 2016 and 1981 GLOFs [up to 5.7 m (fig. S5) and 13.4 m in diameter, respectively (11)].

GLOFs can mobilize boulders, owing to their high discharge and other characteristics that enhance sediment entrainment. Outburst floods, in which a water bore propagates downstream, have a higher capacity to mobilize sediment than a monsoon flood of similar magnitude. This is due to the velocity difference between water flow and entrained bedload, which ensures that the leading edge of the flood will remain relatively bedload free and under transport capacity. This is fundamentally different from run-off–driven floods, which have more smoothly varying hydrographs and sediment loads delivered from outside the channel.

The ability to mobilize the channel-defining coarse sediment determines the degrees to which a flood can incise bedrock and erode the channel banks. The bedrock bed of the observed section of the Bhotekoshi River is covered by a sediment layer of unknown thickness. A flood that does not move the large boulders armoring this sediment mantle therefore cannot cause bedrock incision.
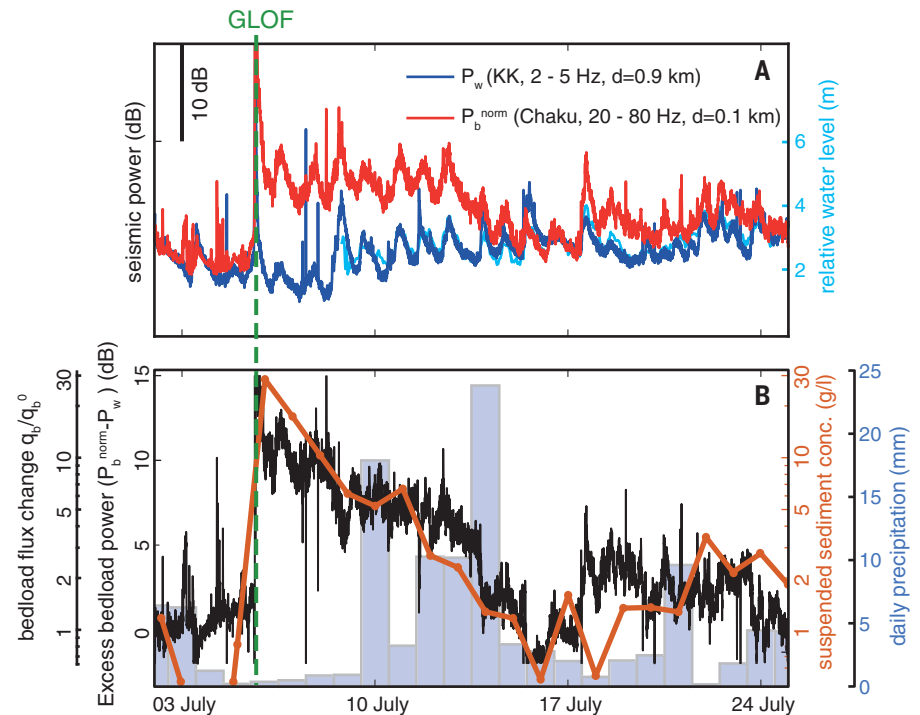
Fig. 4. Sediment dynamics after the GLOF. (**A**) Constraints on bedload transport. The dark blue line shows the seismic power in the 2- to 5-Hz frequency range (P_w) at station KK, a distance (d) of 0.9 km from the river, as a proxy for turbulent flow. The red line shows the seismic power in the 20- to 80-Hz frequency range (P_b^{norm}) at station Chaku, 0.1 km from the river, as a proxy for bedload flux. The light blue line shows the water level relative to the Nepal Department of Hydrology and Meteorology gauge at Barabise. Bedload power has been normalized to the turbulent flow power by using the period before the GLOF. Note that seismic power during the GLOF event itself is off the scale of this plot. (**B**) Excess sediment transport. The black line shows the excess bedload power, obtained by differencing the blue and red series in (A). The GLOF event is off the scale of this plot and is not considered in this analysis. The orange line shows the suspended-sediment concentration from daily samples. The bars show Global Precipitation Monitoring–derived catchment-wide daily precipitation. q_b, bedload flux; q_b^0, background bedload flux.

The impact of the 2016 and 1981 GLOFs on the bedrock below the sediment layer cannot be constrained; however, we can conclude that these GLOFs may have incised bedrock, whereas the monsoon floods since at least 2004 definitely did not.

GLOF-induced disruption of the boulder armor is reflected in increased rates of sediment transport during the 10 days after the 2016 GLOF. We used seismic signals in different frequency ranges from a far-river station and a near-river station to obtain proxies for water flow depth and bedload flux (17, 18) (Fig. 4A and fig. S1). Before the GLOF, the bedload flux and water depth proxies are closely linked. After the GLOF, however, the two proxies show different trends. Whereas the flow depth proxy returns to preflood levels within hours, the bedload transport proxy is increased after the flood and gradually returns to preflood levels over 10 days (Fig. 4B). Daily suspended-sediment concentrations from Barabise show a very similar perturbation, with changes of the same magnitude and time evolution as the estimated excess bedload transport (Fig. 4B), suggest-ing that both fluxes are controlled by sediment availability from the same source. We interpret this as a signal of ongoing reorganization of the channel bed; the return to background levels of sediment transport occurs as easily transportable sediment is removed from the channel and the boulder armor reestablishes. Furthermore, the increase in bedload transport after the GLOF suggests that at most other times the river is under capacity and that bedload transport during the monsoon is typically limited by the delivery of sediment into the channel.

Because of the high discharge threshold for mobilizing the channel-defining boulders, monsoon floods primarily transfer sediment delivered from tributaries and hillslopes without major lateral or vertical erosion in the main channel, and only very large floods cross the threshold for boulder mobilization, perturb the river, and drive erosion. This allows individual floods, including GLOFs and landslide dam outbursts, to have a disproportionate impact on the river channel. The role of GLOFs in driving long-term erosion and hillslope-channel coupling therefore depends

on their frequency and magnitude relative to that of extreme monsoon-driven floods.

The frequency of GLOFs in the central Himalaya is difficult to establish, because records are incomplete and recorded floods may not be correctly identified as GLOFs (3, 23). Nevertheless, GLOFs are relatively common in the Himalaya, with a major flood occurring at least once every 2 years on average (4, 24–26). The Bhotekoshi River has experienced GLOFs in 1935, 1964, 1981, and 2016, suggesting a return period of about 30 years (2). The Bhotekoshi/Sunkoshi catchment has 57 glacial lakes mapped upstream of Barabise (10). These lakes vary widely in size, but the median lake area of 32,600 m^2 is almost twice that of the lake that caused the 2016 flood. Yearly maximum monsoon discharge from a 42-year discharge record at Barabise is typically between 200 and 400 m^3/s, with flood peaks rarely exceeding 500 m^3/s (fig. S9). The estimated GLOF peak discharges at Barabise [700 to 900 m^3/s in 2016 and 2300 m^3/s in 1981 (11)] are larger than the expected 30-year flood discharge of 490 to 560 m^3/s (Fig. 2, fig. S11, and table S4). The impact of individual GLOFs on the Bhotekoshi River dwarfs that of monsoon discharges, and GLOFs occur with sufficient frequency to dominate geomorphic change in the valley.

As a GLOF travels downstream, the flood peak attenuates and the peak discharge decreases, whereas the drainage area and background discharge increase, giving rise to a crossover point where GLOF discharges are no longer anomalous (7, 10) (Fig. 2). Hence, the discrepancy between GLOF discharge and monsoon floods will be particularly dramatic in the high Himalayan headwaters, where the drainage areas are small and GLOFs will have experienced little attenuation (Fig. 2). For the 2016 and 1981 GLOFs, the crossover point with the 30-year monsoon flood was located about 45 and 55 km downstream of the Zhangzangbo confluence, respectively (Fig. 1). If GLOFs are less frequent, then their impact must be measured against larger monsoon floods with a longer return time, moving the crossover point upstream. Conversely, larger GLOFs have a crossover point farther downstream. Probabilistic modeling of glacial lake outbursts throughout the Himalaya suggests that more than 40% of 2359 mapped proglacial lakes could produce GLOFs that match the 100-year discharge about 20 km downstream, whereas large GLOFs may reach as far as 85 km downstream (10). Our observations suggest that, because of their distinct sediment dynamics, GLOFs of such magnitudes will have a disproportionate effect on fluvial erosion in these reaches.

Owing to their magnitude and enhanced ability to mobilize coarse sediment, we propose that LOFs are a fundamental part of the fluvial system and a primary control on fluvial erosion and channel-hillslope coupling, especially in catchments where very coarse sediment creates high thresholds for sediment mobilization, with GLOFs particularly effective in the upper portions of glaciated catchments. Landslide LOFs

likely have a similar impact on channel dynamics and channel-hillslope coupling in landslide-prone regions with steep narrow valleys and abundant coarse sediment, conditions that are common in numerous mountain ranges throughout the world (4, 5).

LOFs directly impact only the channel and adjacent hillslopes, but over the long term, fluvial incision sets the base level for the entire landscape and is ultimately the driver of hillslope erosion; thus, in LOF-prone regions, LOF magnitudes and recurrence intervals may control landscape evolution. As a result, monsoon strength or measures of precipitation may be poor predictors of landscape response in LOF-susceptible regions. Instead, erosion rates may be strongly influenced by nonclimatological LOF drivers such as earthquakes (5, 27, 28) and the climatic factors that affect the size and distribution of glacial lakes, for example, air temperature, variability of the equilibrium line altitude, and, to a degree, the glacial recharge (29, 30). Even where LOF frequency can be linked to precipitation (that is, for landslide lake outbursts), the relationship between fluvial erosion and precipitation will become complicated and nonlinear.

A warming climate is thought to promote glacial lake formation in some areas as retreating glaciers create space for lakes behind abandoned end moraines and increased melting rates supply more water to potential lakes. This, in turn, may increase GLOF frequency and/or magnitude (25, 31–33). The potential for increased GLOF activity in response to climate change therefore not only represents increased risk to communities in these regions but may also strongly affect the pace of landscape change in a way that is not reflected in precipitation-dependent erosion models.

REFERENCES AND NOTES

1. K. Hewitt, "Natural dams and outburst floods of the Karakoram Himalaya," in *Hydrological Aspects of Alpine and High-Mountain Areas*, J. W. Glen, Ed. (IAHS Publication No. 138, International Association of Hydrological Sciences, 1982), pp. 259–269.
2. P. K. Mool, *J. Nepal Geol. Soc.* **11**, 273–280 (1995).
3. International Centre for Integrated Mountain Development (ICIMOD), "Glacial lakes and glacial lake outburst floods in Nepal" (ICIMOD, Kathmandu, 2011).
4. O. Korup, F. Tweed, *Quat. Sci. Rev.* **26**, 3406–3422 (2007).
5. J. E. Costa, R. L. Schuster, *Geol. Soc. Am. Bull.* **100**, 1054–1068 (1988).
6. M. J. Westoby et al., *Earth Sci. Rev.* **134**, 137–159 (2014).
7. D. A. Cenderelli, E. E. Wohl, *Geomorphology* **40**, 57–90 (2001).
8. A. B. Shrestha et al., *Geomatics Nat. Hazards Risk* **1**, 157–169 (2010).
9. N. R. Khanal, J. M. Hu, P. Mool, *Mt. Res. Dev.* **35**, 351–364 (2015).
10. W. Schwanghart, R. Worni, C. Huggel, M. Stoffel, O. Korup, *Environ. Res. Lett.* **11**, 074005 (2016).
11. D. Xu, *GeoJournal* **17**, 569–580 (1988).
12. D. A. Cenderelli, E. E. Wohl, *Earth Surf. Process. Landf.* **28**, 385–407 (2003).
13. D. Higaki, G. Sato, *Glob. Environ. Res.* **16**, 71–76 (2012).
14. C. Huggel, A. Kääb, W. Haeberli, P. Teysseire, F. Paul, *Can. Geotech. J.* **39**, 316–330 (2002).
15. J. S. Kargel et al., *Science* **351**, aac8353 (2016).
16. K. Roback et al., *Geomorphology* **301**, 121–138 (2017).
17. F. Gimbert, V. C. Tsai, M. P. Lamb, *J. Geophys. Res. Earth Surf.* **119**, 2209–2238 (2014).
18. V. C. Tsai, B. Minchew, M. P. Lamb, J. P. Ampuero, *Geophys. Res. Lett.* **39**, L02404 (2012).
19. A. Burtin, L. Bollinger, J. Vergne, R. Cattin, J. L. Nábělek, *J. Geophys. Res. Solid Earth* **113**, B05301 (2008).
20. P. Chatanantavet, K. X. Whipple, M. A. Adams, M. P. Lamb, *J. Geophys. Res. Earth Surf.* **118**, 1161–1176 (2013).
21. D. A. Cenderelli, B. L. Cluer, "Depositional processes and sediment supply in resistant-boundary channels: Examples from two case studies," in *Rivers Over Rock: Fluvial Processes in Bedrock Channels*, K. J. Tinkler, E. E. Wohl, Eds. (Geophysical Monograph Series, vol. 107, American Geophysical Union, Washington, DC, 1998), pp. 105–131.
22. A. C. Brayshaw, *Geol. Soc. Am. Bull.* **96**, 218–223 (1985).
23. Rastriya Samachar Samiti, "Heavy rain brings massive flood to Bhotekoshi River," *Himalyan Times*, 6 July 2016; https://thehimalayantimes.com/nepal/heavy-rain-brings-massive-flood-bhotekoshi-river.
24. J. D. Ives, R. B. Shrestha, P. K. Mool, "Formation of glacial lakes in the Hindu Kush-Himalayas and GLOF risk assessment" (ICIMOD, Kathmandu, 2010).
25. A. Lutz, W. W. Immerzeel, S. R. Bajracharya, M. Litt, A. Shrestha, "Impact of climate change on the cryosphere, hydrological regimes and glacial lakes of the Hindu Kush Himalayas: A review of current knowledge" (ICIMOD Research Report 2016/3, ICIMOD, Kathmandu, 2016).
26. D. R. Rounce, A. C. Byers, E. A. Byers, D. C. McKinney, *Cryosphere* **11**, 443–449 (2017).
27. W. Schwanghart et al., *Science* **351**, 147–150 (2016).
28. J. D. Bricker et al., *Mt. Res. Dev.* **37**, 5–15 (2017).
29. S. G. Evans, J. J. Clague, *Geomorphology* **10**, 107–128 (1994).
30. K. Hewitt, J. Liu, *Phys. Geogr.* **31**, 528–551 (2013).
31. S. R. Bajracharya, P. Mool, *Ann. Glaciol.* **50**, 81–86 (2009).
32. T. Bolch et al., *Science* **336**, 310–314 (2012).
33. Y. Chen, C. Xu, Y. Chen, W. Li, J. Liu, *Quat. Int.* **226**, 75–81 (2010).

SUPPLEMENTARY MATERIALS

www.sciencemag.org/content/362/6410/53/suppl/DC1
Materials and Methods
Figs. S1 to S12
Tables S1 to S6
References (34–38)

Science

Glacial lake outburst floods as drivers of fluvial erosion in the Himalaya

Kristen L. Cook, Christoff Andermann, Florent Gimbert, Basanta Raj Adhikari and Niels Hovius

A sudden outburst of erosion
Glacial lake outburst floods (GLOFs) are exactly what they sound like. The sudden emptying of a glacial lake in high-topography regions like the Himalaya can quickly destroy everything in its path. Cook *et al.* intercepted a GLOF in the Bhotekoshi and Sunkoshi river valleys in central Nepal as they were monitoring the region in the aftermath of the 2015 Gorkha earthquake. They found that a massive amount of erosion occurred during the outburst flood, which suggests that GLOFs may be the primary factor in landscape evolution for these regions.
Science, this issue p. 53

ARTICLE TOOLS	http://science.sciencemag.org/content/362/6410/53
SUPPLEMENTARY MATERIALS	http://science.sciencemag.org/content/suppl/2018/10/03/362.6410.53.DC1
REFERENCES	This article cites 31 articles, 6 of which you can access for free http://science.sciencemag.org/content/362/6410/53#BIBL
PERMISSIONS	http://www.sciencemag.org/help/reprints-and-permissions

Use of this article is subject to the Terms of Service

Supplementary Materials for

Glacial lake outburst floods as drivers of fluvial erosion in the Himalaya

Kristen L. Cook*, Christoff Andermann, Florent Gimbert, Basanta Raj Adhikari, Niels Hovius

*Corresponding author. Email: klcook@gfz-potsdam.de

This PDF file includes:

Materials and Methods

Lake volume

We estimated the lake volume using a scaling relationship between lake area and volume *(14)*, $V = 0.104 * A^{1.42}$. The lake area was measured using Oct 2015 satellite imagery and assuming that the lake was at its maximum water level.

Seismic data

Seismic stations were installed in June 2015 and consist of either a Nanometrics Trillium Compact 120s broadband seismometer (Hindi, Chaku, Listi) or a Mark L-4C 1 Hz 1 component geophone (Chakam, Tyanthali, KK) and an Omnirecs Cube ext[3] data logger. Stations were installed in soil approximately 0.5 m below the surface. Sampling frequency was 200 Hz. For the waveform timeseries (Fig. 1C), we applied a bandpass filter (1-90 Hz) and manually picked the arrival times of the two GLOF pulses. The velocity of each pulse was estimated with a linear distance vs time fit. The total duration of the flood was determined manually.

We calculated power spectra at four stations (Hindi, Chaku, Tyanthali, and KK) for both of the GLOF pulses, the post-GLOF period (July 7), a monsoon flood (August 5), and the pre-monsoon period (May 12) (Fig. S3). Each spectrum is calculated over three minutes, with the times shown in Fig. S3.

Estimates of changes in water discharge and bedload flux from the seismic signal
We inferred river flow depth variations from the lower frequency content (2 to 5 Hz) of ground motion variations at seismic station KK, which is 0.9 km from the river. This is far enough to maximize sensitivity to turbulent-flow-induced noise and thus flow depth variations *(17)*, but close enough to still be sensitive to the moderate river-induced noise under the usual river flow depths before and after the flood (Fig. 4A, blue curve). The seismic-derived flow depth time series is consistent with data from a water level gauge that was installed by the Nepal DHM (Department of Hydrology and Meteorology) in Barabise following the flood; the seismic data captures both the diurnal variations and mean trends in water level. We exclude the GLOF itself from this analysis, and assume that discharge is continuous downstream and varies smoothly in time, so that the relative discharge in two reaches 3 km apart will behave the same way. We inferred bedload transport changes from the higher frequency content (20 to 80 Hz) of seismic ground motion variations at station Chaku, which is 0.1 km from the river, a distance that maximizes sensitivity to bedload induced noise *(17)* (see red curve of Fig. 4A).

We selected the 2-5 Hz and 20-80 Hz frequency ranges based on models of seismic noise generated by turbulent flow *(17)* and bedload transport *(18)*, which are consistent with observational evidence *(34, 35)*. We applied these models to the Bhotekoshi using the parameters shown in table S5, yielding predicted frequency spectra for Chaku and KK stations (Fig. S1). When possible, we used values measured for the Bhotekoshi (i.e. channel width, slope, water depth, station distance) otherwise we adopted the values used for the Trisuli River in *(17)*. The Trisuli River is located 70 km west of the Bhotekoshi, and has hydrological and geomorphic characteristics similar to the latter. We have added a parameter for grain roughness to the models; we observe that the largest clasts in the channel are not transported (aside from during the GLOF), so the roughness should be parameterized by a larger grain size than we used to calculate the bedload-generated power.

Theory predicts that changes in channel geometry (bed roughness, channel cross-section) could change the seismic power induced by turbulent-flow *(17)*, which could bias our measurements of excess bedload-induced noise. However, if changes to these factors from pre- to post- GLOF were significantly affecting seismic noise power, as observed in *(36)*, then an abrupt pre- to post- GLOF shift in the 2-5 Hz power should be observed, which is not the case. The 2-5 Hz time series (Fig. 4A) does not react to the passage of the GLOF – the diurnal minimum the day before the GLOF and the diurnal minimum the day after the GLOF are very similar, with the slight decrease expected following several dry days. Thus, we conclude that our reported pre- to post-GLOF seismic observations are not significantly affected by changes in channel geometry. This can be explained by the fact that, unlike the very close station to river range (<4 m) used in *(36)*, our seismic stations are placed much farther away (100 m to 900 m) from the channel, and are thus sampling a much longer (10^2-10^3 m) stretch of the channel. Changes must be systematic over this stretch of channel to have an important impact on the generated seismic noise.

Each seismic time series provides a record of relative changes in discharge and bedload transport, but we do not calculate absolute values for either of them. We expect a covariance between the two seismic time series because sediment transport depends on discharge, but some degree of overlap between the water and sediment frequency ranges could also contribute. In the period prior to the GLOF and following the recovery from the GLOF, we observed that the discharge proxy and the bedload proxy do coevolve. This indicates that for a given amount of turbulence-induced noise, under normal conditions there is an expected amount of bedload-induced noise. We consider this expected amount of bedload-induced noise to reflect the background monsoonal bedload flux (q_b^0). An increase in the bedload-induced noise relative to the turbulence-induced noise then reflects an increase in bedload flux above this monsoonal background bedload flux. By normalizing the bedload-induced power by the turbulence-induced power, we can quantify the excess bedload seismic noise (Fig. 4B). Note that, because decibels (dB) are a logarithmic unit, subtraction in dB is equivalent to division of seismic power.

The excess bedload noise can then be related to an increase in bedload flux using the scaling found in *(18)*: $P_b \sim D^3 q_b$, where P_b is the bedload seismic power, D is the bedload grain size, and q_b is the bedload flux. We assumed that the grain size of transported bedload is similar prior to and after the GLOF (we excluded the GLOF itself from this analysis). A change in seismic power is therefore directly proportional to a change in bedload flux, so a 15 dB increase in seismic power corresponds to a factor of 30 increase in sediment flux (note that decibels are a logarithmic unit).

Our assumption of constant grain size is supported by time lapse photographs that do not show major changes to the channel or mobile boulders during the post-flood period. From a theoretical standpoint, we don't expect that the grain size of the moving bedload is higher after the flood because the discharge quickly returned to levels that cannot transport large clasts. Because the channel contains a very wide range of grain sizes, the control on the grain size of transported material will be set by the combination of sediment supply and discharge. If there is a grain size change, we expect it to be a reduction in the median transported grain size during the post-flood period and then a gradual increase. We argue that the post-flood period contains elevated bedload transport because of an increase in sediment supply. Typically in the channel the smaller grains should be underrepresented because they are so easy to transport that they are quickly exported downstream. With a sudden increase in sediment supply, but no increase in transport capacity, the larger barely mobile grains should

3

move at the same rate (because they are limited by mobility rather than supply), while transport of the small mobile grains will increase dramatically and then drop off as supply is exhausted, exactly as we see in the suspended sediment data.

Given the lack of data on the distribution of moving grains through time, we conclude that holding grain size constant is the only reasonable choice. It is also the conservative choice – if grain size evolves as we predict, then we are underestimating the change in flux (as a smaller grain size will require a higher flux to maintain the same seismic power).

During the passage of the GLOF, there are several factors that will influence the relationship between discharge and seismic noise generation. The mobilization of bed material likely changed the roughness of the channel, and changes to the channel cross section may have influenced the generation of turbulence. In addition, the mobilization of boulders indicates that the transported grain size increased during the GLOF, strongly influencing the scaling between seismic power and bedload flux. For these reasons, we do not attempt to use the magnitudes of the seismic signals to constrain discharge or sediment flux during the GLOF itself.

Terrestrial Lidar
Lidar data was collected with a Riegl VZ6000 long range laser scanner in October 2015, March 2016, and November 2016; the pre-flood lidar surveys were focused on hillslope processes rather than fluvial change, so the survey locations were not influenced by the distribution of changes in the channel, although there is a bias towards locations where the river bed can be observed from the road above. The data were processed using RiSCAN Pro and the scans were minimally filtered - intermediate and first returns were excluded, but no other filtering or vegetation removal was done. The scans were aligned using the multistation adjustment algorithm in RiSCAN Pro. The reliability of the alignment process can be assessed by comparing areas that did not change between scans, and errors are 3-4 orders of magnitude smaller than the measured changes. The scans at Barabise were collected with a Faro Focus 330 laser scanner. For each survey period, scans from two positions were aligned using the Faro Scene software cloud matching algorithm, and the resulting models were imported into Riscan Pro and aligned with each other using the multistation adjustment algorithm.

Change between scan periods was calculated using the M3C2 cloud/cloud distance algorithm *(37)*, which calculates distances in the direction of the best fit normal to the point cloud surface. We used multiscale normals from 1 to 9 meters in 2 meter increments and a projection cylinder with a diameter of 1-2 m, depending on the scan resolution. The change maps were filtered to remove points with high standard deviation, which are related to vegetation. The lidar scans capture the water surface, so changes to the bed elevation are not precise. However, discharge in the Bhotekoshi was higher during the November 2016 scanning period than during the earlier scan periods, so a lower water surface at this time requires a lower bed elevation, and the measured changes provide a minimum constraint on bed lowering.

Time lapse cameras
Time lapse photographs were taken with Bushnell NatureView cameras set to take photographs every 30 or 60 minutes. The camera at Barabise was blocked by debris for 10 days following the outburst flood. Time-lapse photographs indicate that the channel experienced little modification prior to the outburst and throughout the rest of the monsoon

season after the outburst flood (Figure S4). The geomorphic changes that we observe over the monsoon season can therefore be dominantly attributed to the outburst and not to prior or succeeding precipitation driven floods.

Channel width and landslide mapping
Regional mapping was done using Rapideye data, which consist of RGB images with 5 m resolution. When possible, we selected images from October or November of each year from 2009 to 2016. By limiting the images to these months, we reduced errors from changes in leaf density, vegetation growth, and discharge. The area of interest is covered by two tiles, and for the 2009/2010 mapping, we used a 2009 image for the northern tile and a 2010 image for the southern tile, as simultaneous high quality images were not available for both tiles. For changes in the 2012 monsoon season, we used an image from March 2013 for one tile, as an image from fall 2012 was not available (Table S3).

For each image, we manually mapped the margins of the active channel, defined by the absence of vegetation. We also mapped landslides associated with the river channel. Landslides are identified by the removal of vegetation, and they are associated with the channel if the zone of failure is connected to the channel. Landslides with scars higher on the hillslopes were not included, even if they delivered debris to the channel. The purpose of this distinction is to isolate the mass wasting events that are related to bank erosion and undercutting by the active channel. This distinction was straightforward for most years, but in 2015 following the Gorkha earthquake, the large volume of landslides and landslide debris in the landscape made the attribution less certain. The relationship between several of the observed landslides and the outburst flood was corroborated by accounts from local people. We did not calculate landslide volumes because many of the bank collapse landslides are unlikely to exhibit typical area-volume scaling, so we prefer to avoid this additional source of uncertainty and discuss only landslide area.

Suspended sediment concentrations
Suspended sediment was obtained from samples collected daily from a suspension bridge upstream from Barabise (point labelled Barabise cross section in Fig. 1), using a fish sampler in the center of the channel. For each sample, 3 liters of water were collected and immediately filtered through 0.22 μm filter paper. The sediment was washed off the filter paper, dried in an oven, and weighed.

Precipitation
Reported daily precipitation values are mean catchment precipitation (Barabise upstream) from GPM IMERGHH v4, 10 km and 0.5 h resolution, compiled to daily resolution.

River discharge and flood frequency analysis
We used long term discharge records from Barabise (station 610, 42 years), Pachuwarghat (station 630, 51 years), and Khurkot (station 652, 38 years), provided by the Nepal Department of Hydrology and Meteorology, and a 5 year record provided by the Upper Bhotekoshi hydropower project management. We removed years with clearly anomalous hydrographs prior to the analysis (Figure S9). The resulting records yield well-behaved probability density distributions (Figure S10).

For extreme value statistics, we fitted to the Laplace, Wakeby, and the Generalized Logistic Extreme value distributions using the R-software package extremeStat *(38)*. We selected these three distributions according to the goodness of fit defined by the RMSE (root mean

square error) for the data from Barabise. To be consistent, we used the same distributions for the other stations. We used the functions distLextreme(annualMax) for fitting annual maxima discharge based on L-moments to derive the annual return periods and used the distLexBoot(distributions, conf.lev=0.5, n=10) function to estimate the 25 and 75 % quantile uncertainty envelopes with bootstrapping (Figure S11). The values given in the text are the range of the 25th and 75th quantiles for all three distributions.

The discharge record from the hydropower station was too short to yield meaningful return period discharges. However, a comparison between the hydropower station and Barabise, 20 km downstream, shows that the two records are well-correlated (Figure S12), suggesting that the discharge at Barabise is a reasonable predictor of discharge upstream.

Discharge calculation

We estimated the peak discharge (Table S1) of the outburst flood at Chaku and Barabise using channel cross sections constructed from points measured above water with a Faro Focus 330 laser scanner combined with measurements of the channel bottom from profiles with a SonTec M9 ADCP. The peak water level was estimated using flood marks and the scan data, and the cross section area, perimeter and hydraulic radius were then calculated. We then used Manning's equation to estimate the peak discharge. We used discharge measured with the ADCP in November 2016 to estimate the appropriate value of Manning's n. At other locations along the channel, we scanned the cross sections with the Faro Focus 330, but have only the portion of the cross section above the November 2016 water level. We assumed a maximum depth of 1 m below the November 2016 water surface at the Borderlands cross section, and used only the November 2016 water surface as the channel base at Khukundol. This reduced the area used in the discharge calculations, making the estimates more conservative. The flow velocities calculated were consistent with flood velocities independently constrained by the seismic data. Uncertainties shown in Fig. 2 and Tables S1 and S4 were estimated based on uncertainties in the high water elevations, the channel slope, and the roughness. Uncertainties are asymmetric because the reported values were calculated using more conservative values for roughness and high water elevation. Reported uncertainties do not include the potential impacts of cross section changes during the flood, which may be significant.
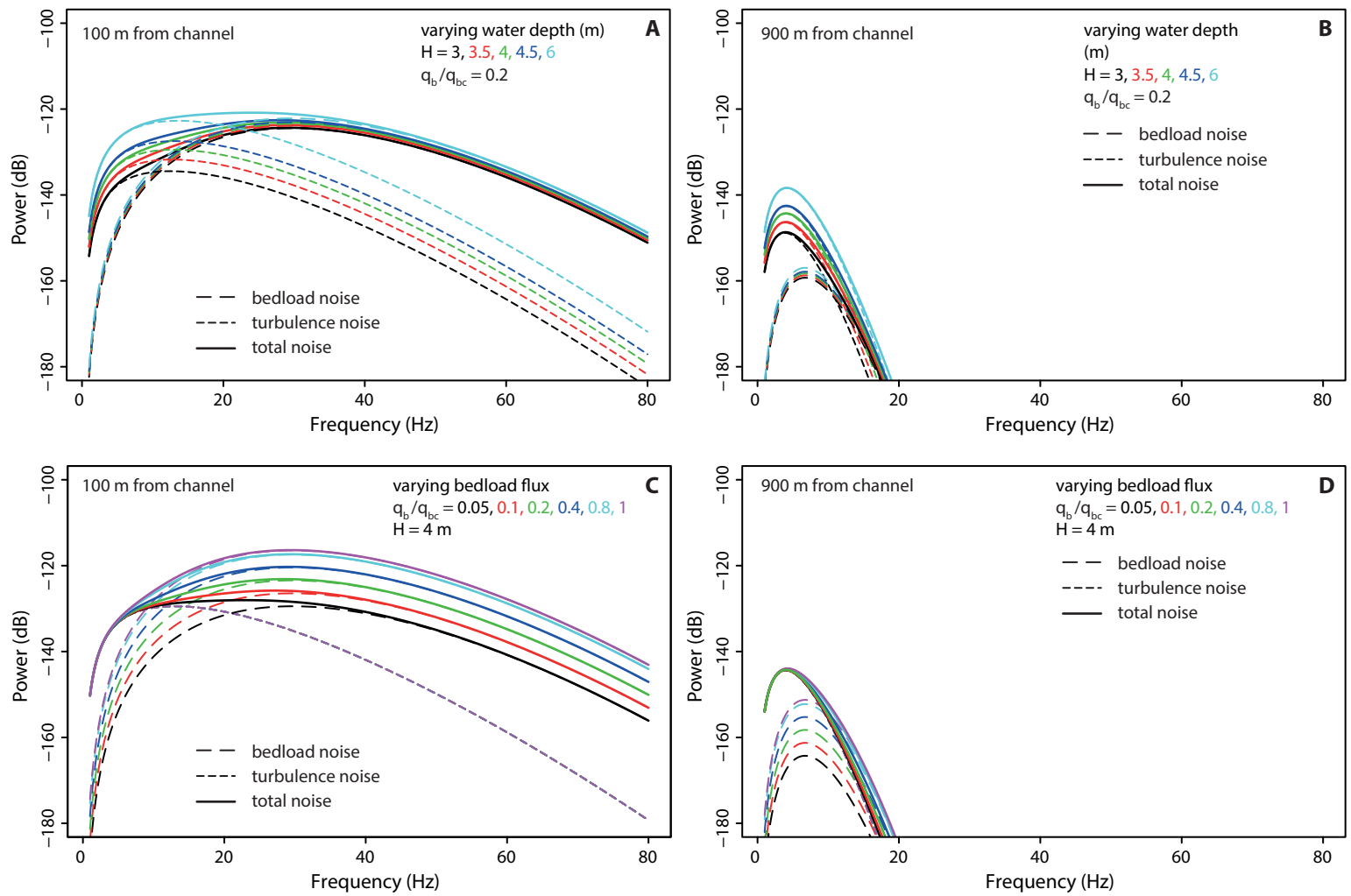
Fig. S1.

Fig. S1. Spectra calculated using models for seismic noise generated by turbulence (15) and bedload transport (16) for stations 100 m from the source (A, C) and 900 m from the source (B, D). Parameters used are listed in Table S5. Short dash lines are the predictions of the turbulence model, long dash lines are the predictions of the bedload model, and solid lines are the predicted total power. (A) and (B) show the predicted spectra for varying water depths. (C) and (D) show the predicted spectra for varying bedload flux, paramaterized as the ratio of bedload flux to transport capacity.
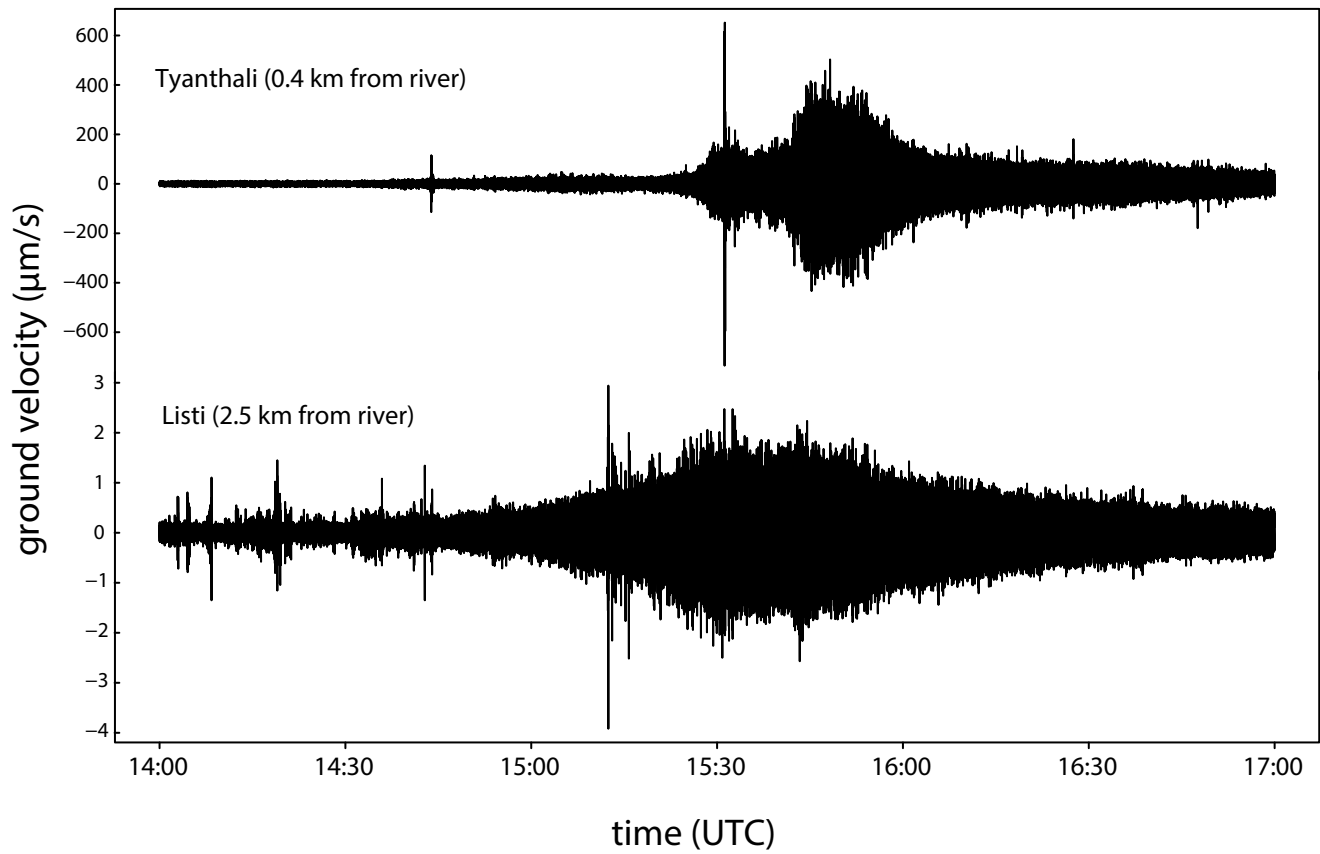
Fig. S2.

Fig. S2. Seismic waveforms at Tyanthali station, close to the river and Listi station, far from the river. The close-to-river stations record two distinct pulses of seismic energy, but this is not observed at the far-from river stations.
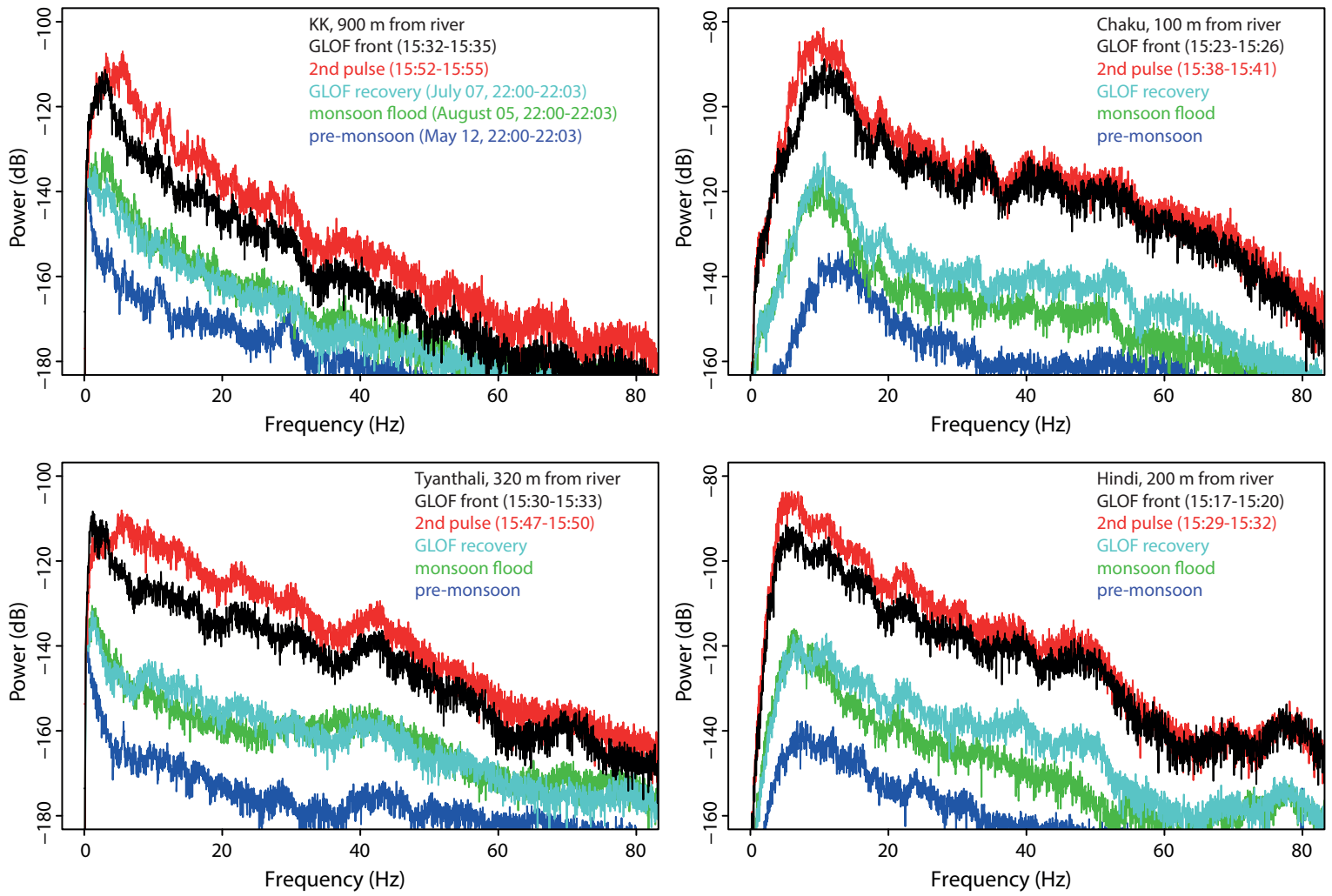
Fig. S3. Power spectra for five different types of event: the GLOF front (black), second GLOF pulse (red), two days post-GLOF (July 07, aqua), monsoon flood (August 05, green), and pre-monsoon (May 12, blue). Each spectra is calculated over 3 minutes and the times are given in the figure legends. For the three non-GLOF events, the same time window was used at all stations.
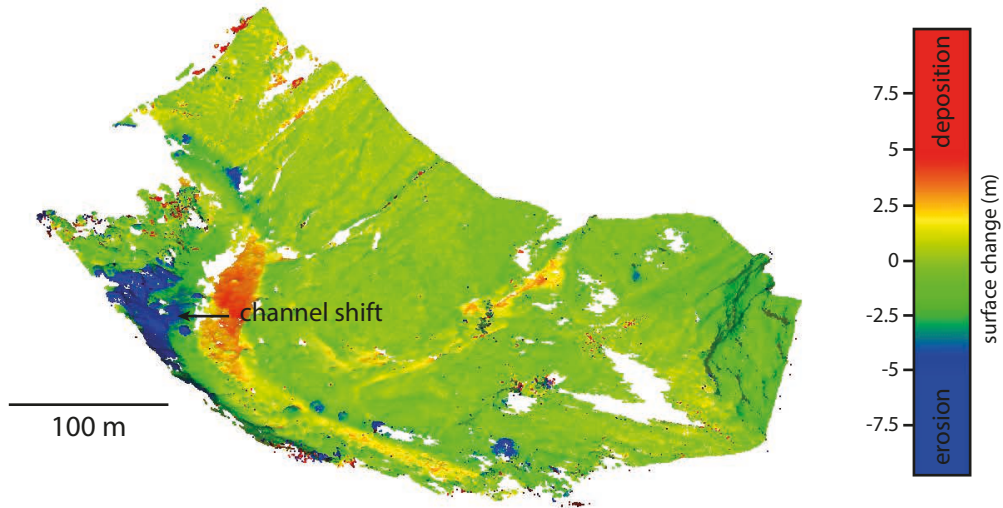
Fig. S4.

Fig. S4. Examples of landslides (A-D) and bank erosion (E-F) caused by the outburst flood. Photos in (A), (B), (E), and (F) courtesy of Bhairab Situala.
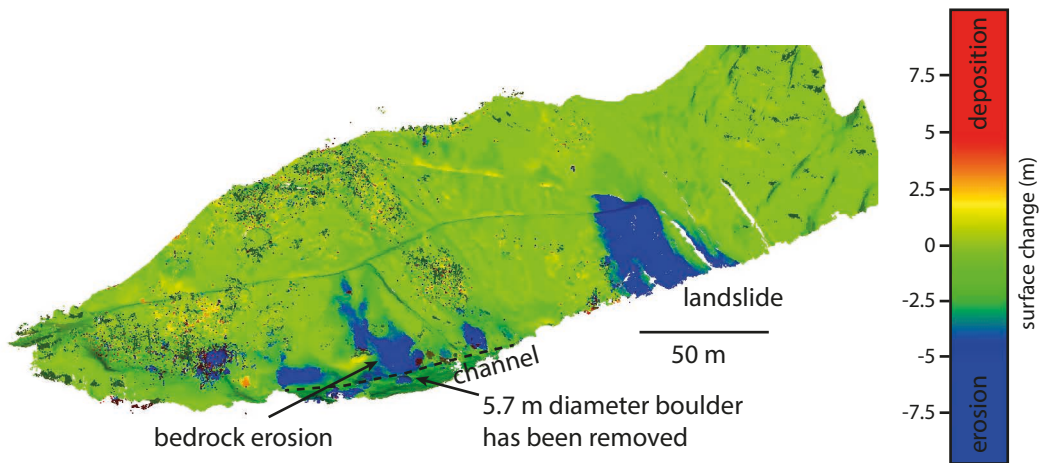
Fig. S5. Change maps calculated from repeat terrestrial lidar scans
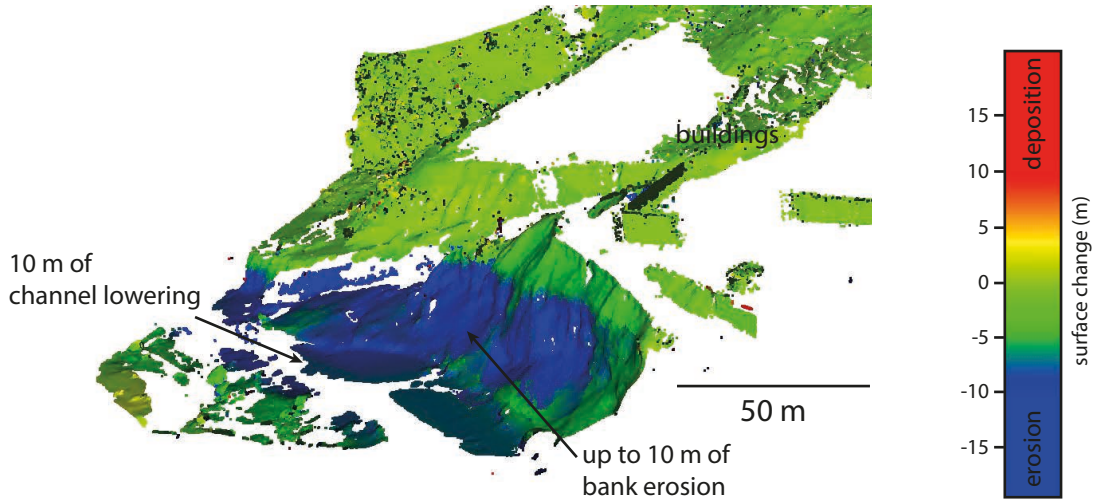
Reach number 1: Khukundol, view looking downstream

Reach number 2: Hindi, view looking downstream

Reach number 3, Listi road bridge. The view is looking obliquely upstream. Changes include flood-induced mass wasting, channel lowering, bedrock wall erosion, and the removal of a 5.7 m boulder.
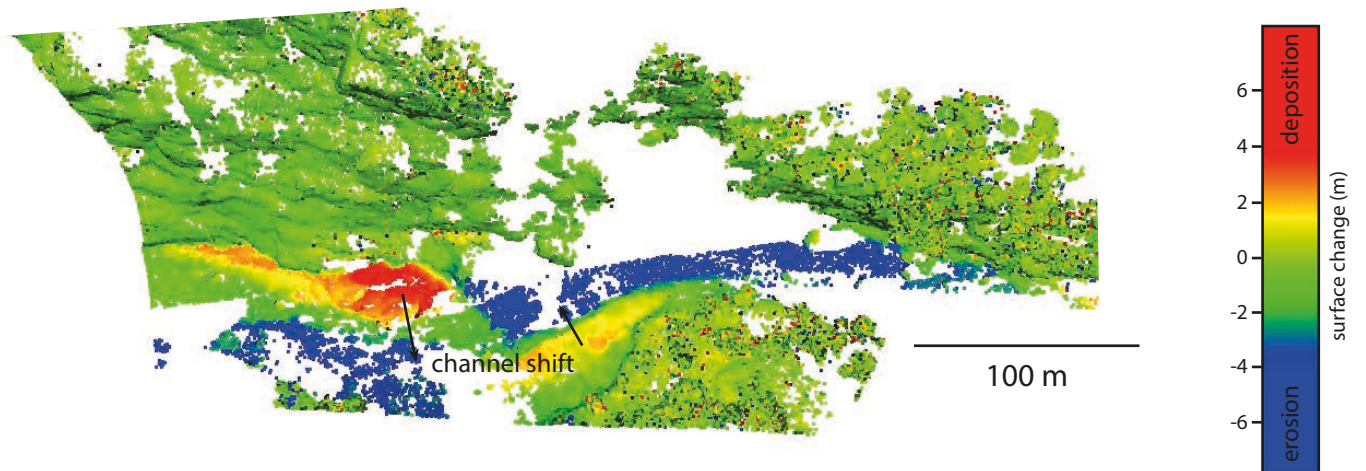
Reach number 4: upstream Chaku, view looking obliquly down, flow is from right to left.
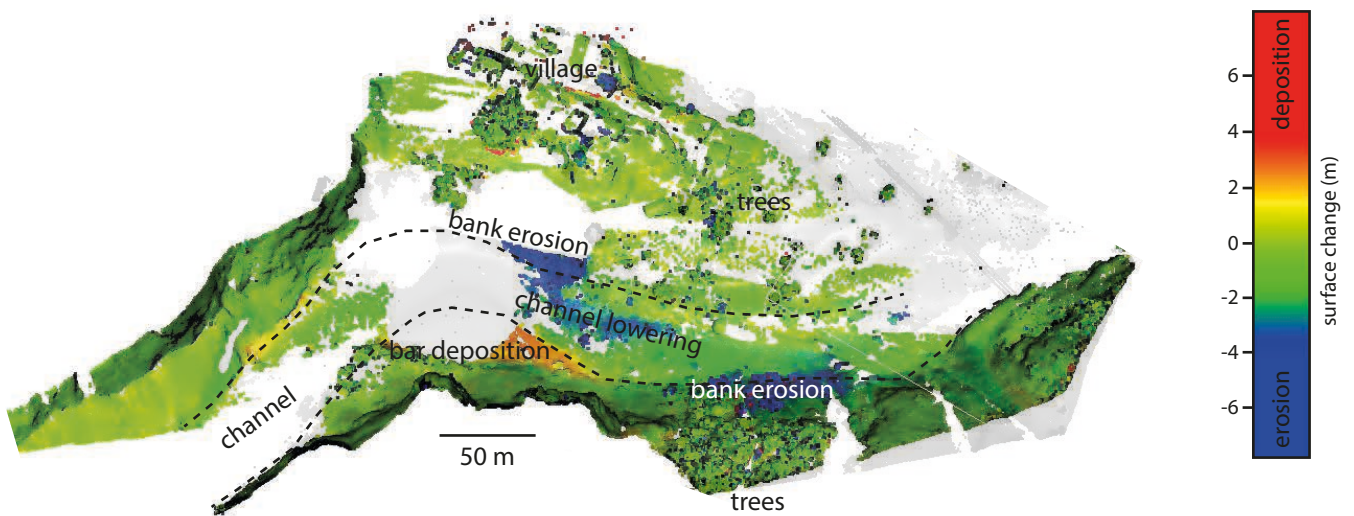
Reach number 5, Chaku: The view is from above, slightly oblique, flow is left to right. For orientation, a smoothed surface calculated from the November 2016 scans is shown. Changes include channel lowering, bank erosion, and bar deposition.

Reach 6a

125 m

surface change (m)

deposition

9

6

3

0

-3

-6

-9

erosion

bank erosion

new building

channel shift

N

Reach number 6: Chaku Downstream. The scanned reach is over 1 km long, so it has been split into two parts and rotated to make the changes more visible. 6a is viewed looking upstream, 6b is viewed looking north, upstream is to the right. Reach 6b is the downstream continuation of reach 6a, an area of overlap is included for orientation.

Reach 6b

landslide

channel

N

75 m

channel

overlap with reach 6a

deposition

3

2

1

0

-1

-2

-3

erosion

surface change (m)

thick vegetation

bank erosion

channel

landslide

30 m

Reach number 7: Kahole Khole. View looking downstream. This reach is heavily vegetated, causing the high variability on the slopes and the missing data throughout the scene. For orientation, the change map is overlain on a smoothed surface calculated from the November 2016 scan and the channel margins are indicated.
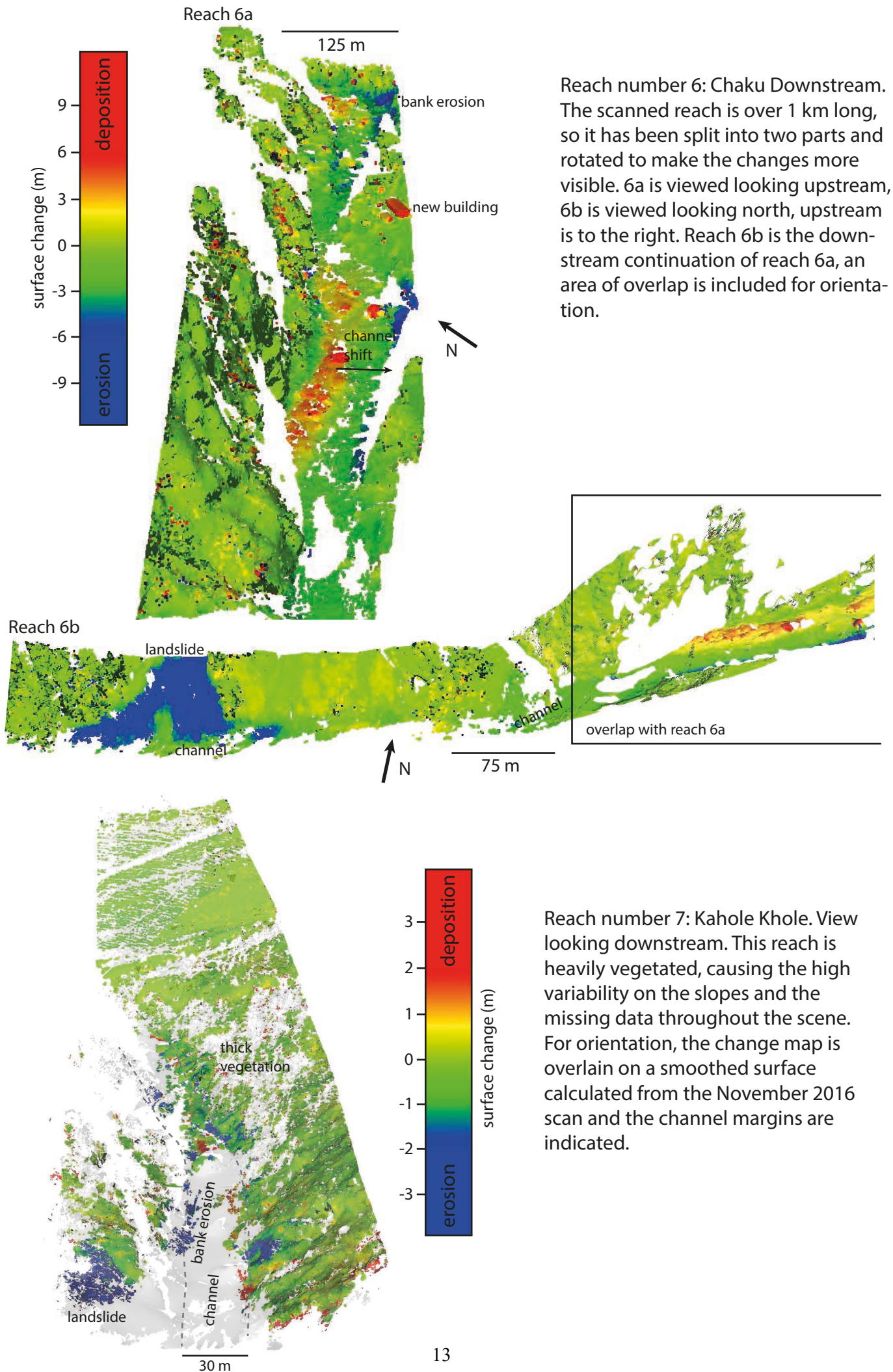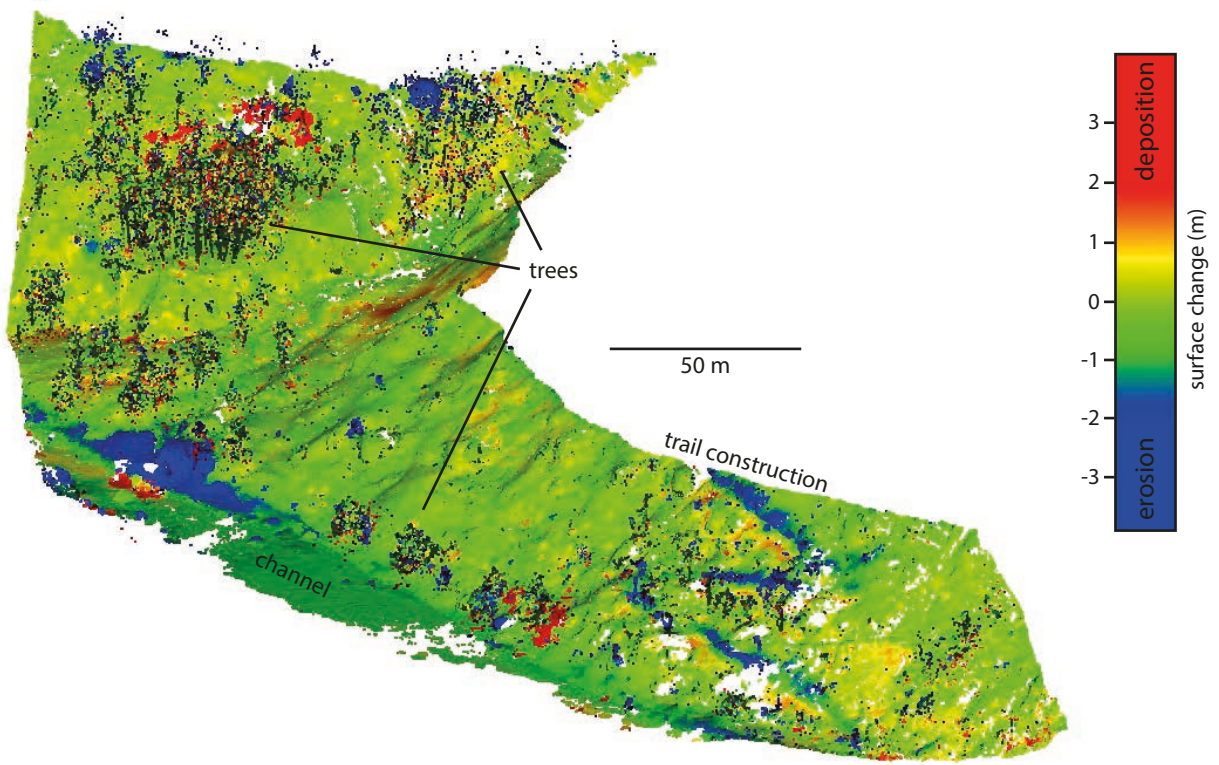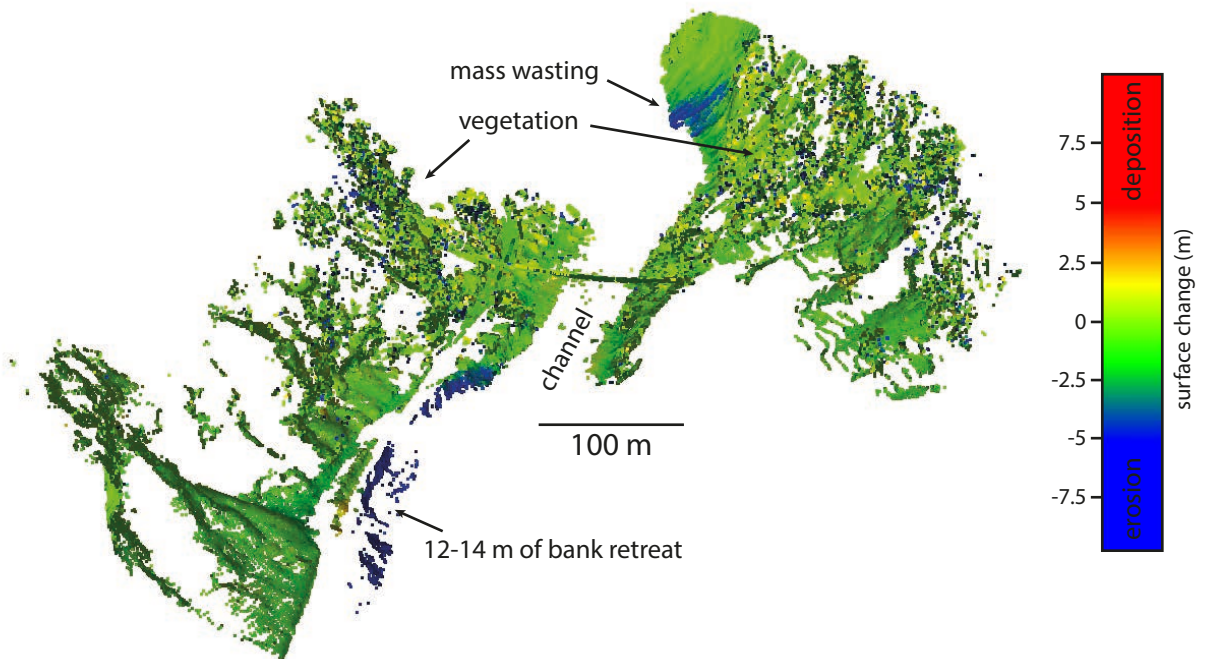
13

Reach number 8: Borderlands. View looking downstream.

Reach number 9: Barabise. View looking downstream. This reach was scanned with a Faro Focus 330 scanner, which does not capture the water surface.
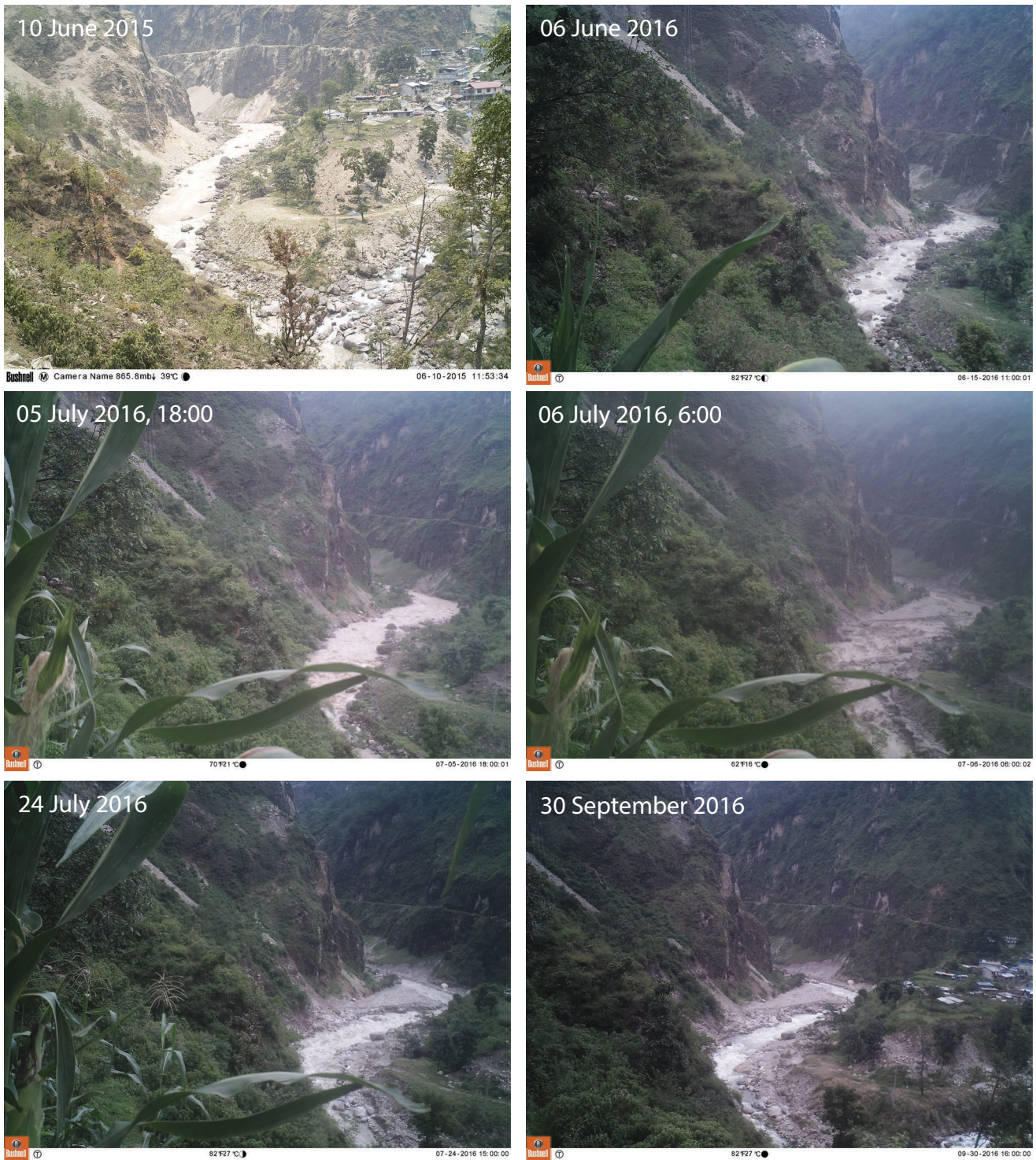
Fig. S6.

Fig. S6. Time lapse photographs looking upstream at Chaku. The photographs illustrate the adjustment to the channel in the outburst flood on the night of 05-06 July, 2016, as well as the lack of change in the channel during a period prior to the outburst flood (10 June, 2015 to 05 July, 2016) as well as during the rest of the 2016 monsoon after the outburst flood.

Fig. S7. Examples of boulder armoring. (A) time-lapse photographs from Barabise. The channel is lined with boulders that remain immobile through the monsoon but are removed by the outburst flood. Photos have been rectified so they have the same scale and perspective. (B) examples of boulder bank armoring on the Bhotekoshi near Chaku and three other rivers in the Nepal Himalaya.

Fig. S8. Google earth images showing the stability of the channel and boulders. (a-b) images of the Bhotekoshi at 27.880°, 85.907° from 2004 to 2013, with selected stable boulders from 2.5 to 5 m in diameter indicated with arrows.. This reach was modified by bridge construction in 2014. (c-e) images of the Bhotekoshi at 27.814°, 85.882° from 2004 to 2016. Selected stable boulders from 2 to 4 m in diameter are indicated with arrows. Water depth varies between the images. A post-GLOF high resolution image is not available.

Fig. S9
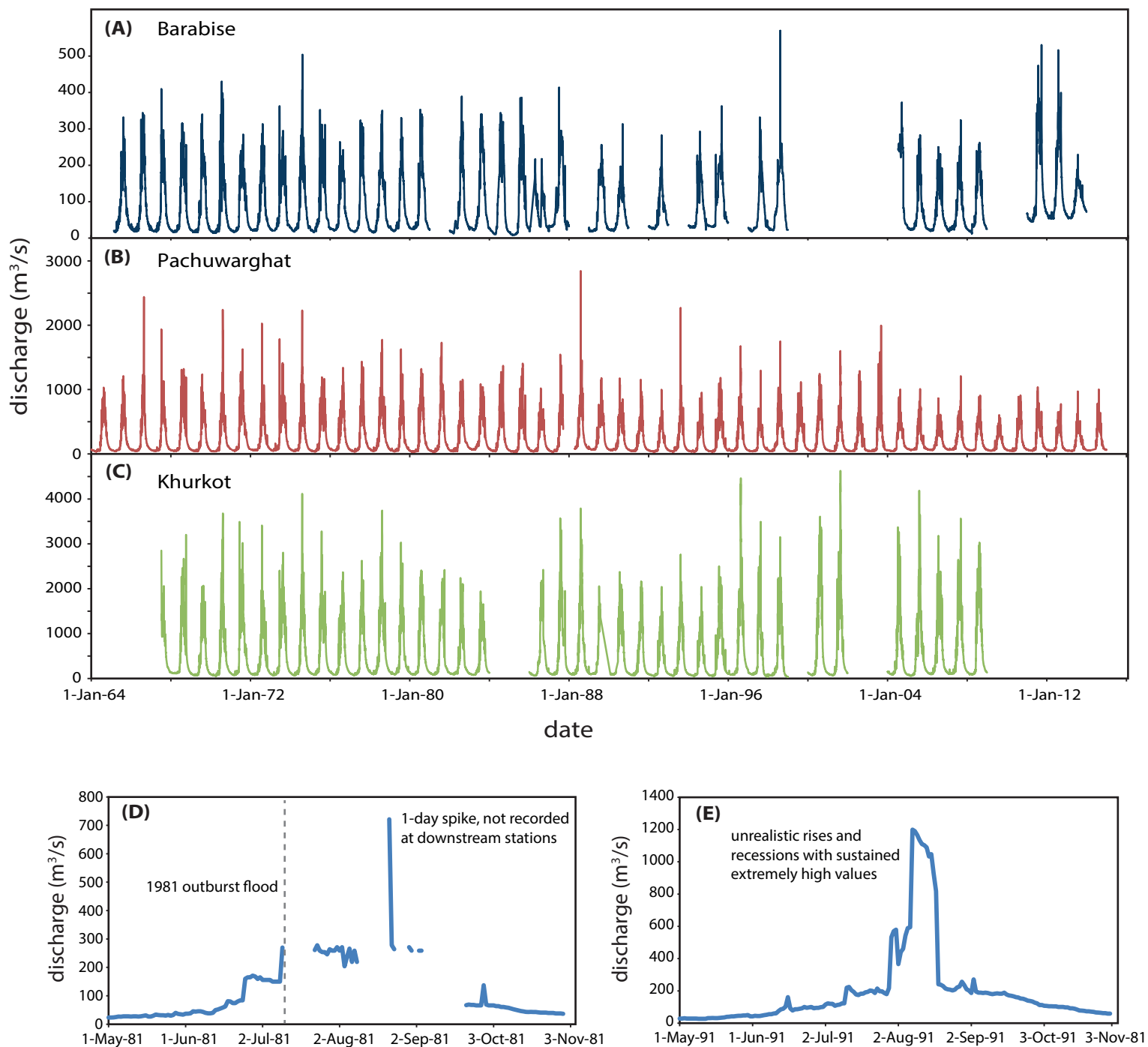
Fig. S9. (A-C) DHM discharge records used in the monsoon flood frequency analysis after the removal of anomalous years (for Barabise: 1981, 1988, 1991, 1993, 1996; for Khurkot: 1984, 1985, 1999, 2002). (D-E) examples of anomalous data removed from the discharge time series, both from Barabise station. Both records show tell-tale signs of gauging problems. (D) the 1981 record does not record the 1981 outburst flood - it has a data gap starting the day of the flood, followed by unrealistic data and numerous additional gaps, suggesting damage to the gauge and likely changes to the cross section. (E) the very large and abrupt changes to the discharge in 1991 suggest problems with the rating curve.

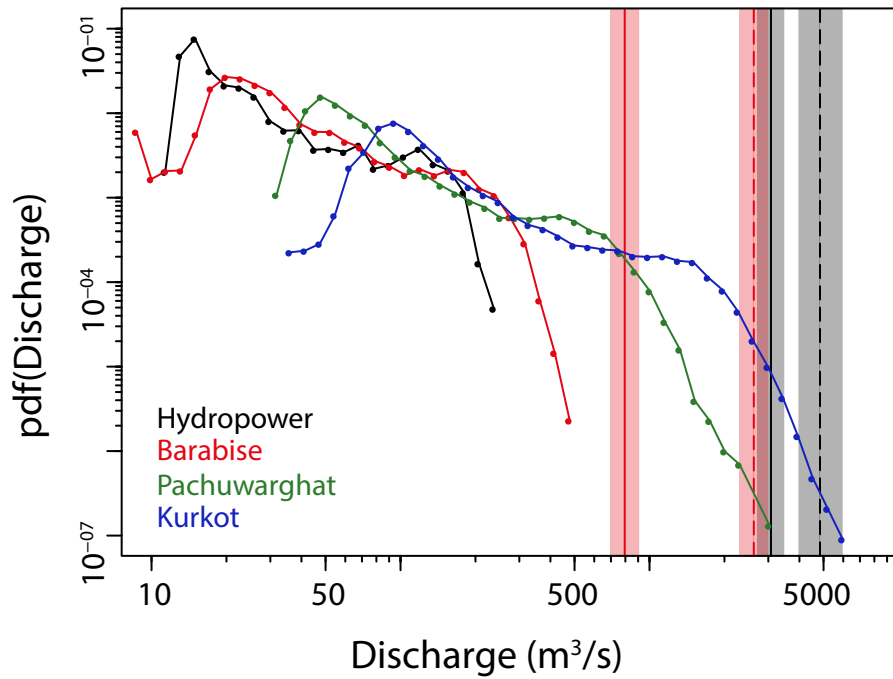Fig. S10. probability density distributions of daily discharge values for four gauging stations along the Bhotekoshi/Sunkoshi River. The discharge values for the 2016 GLOF at Barabise and the hydropower station are indicated with red and black lines, respectively. The discharge values for the 1981 GLOF are indicated with dashed lines. The shading shows approximate uncertainty bounds.

Fig. S11
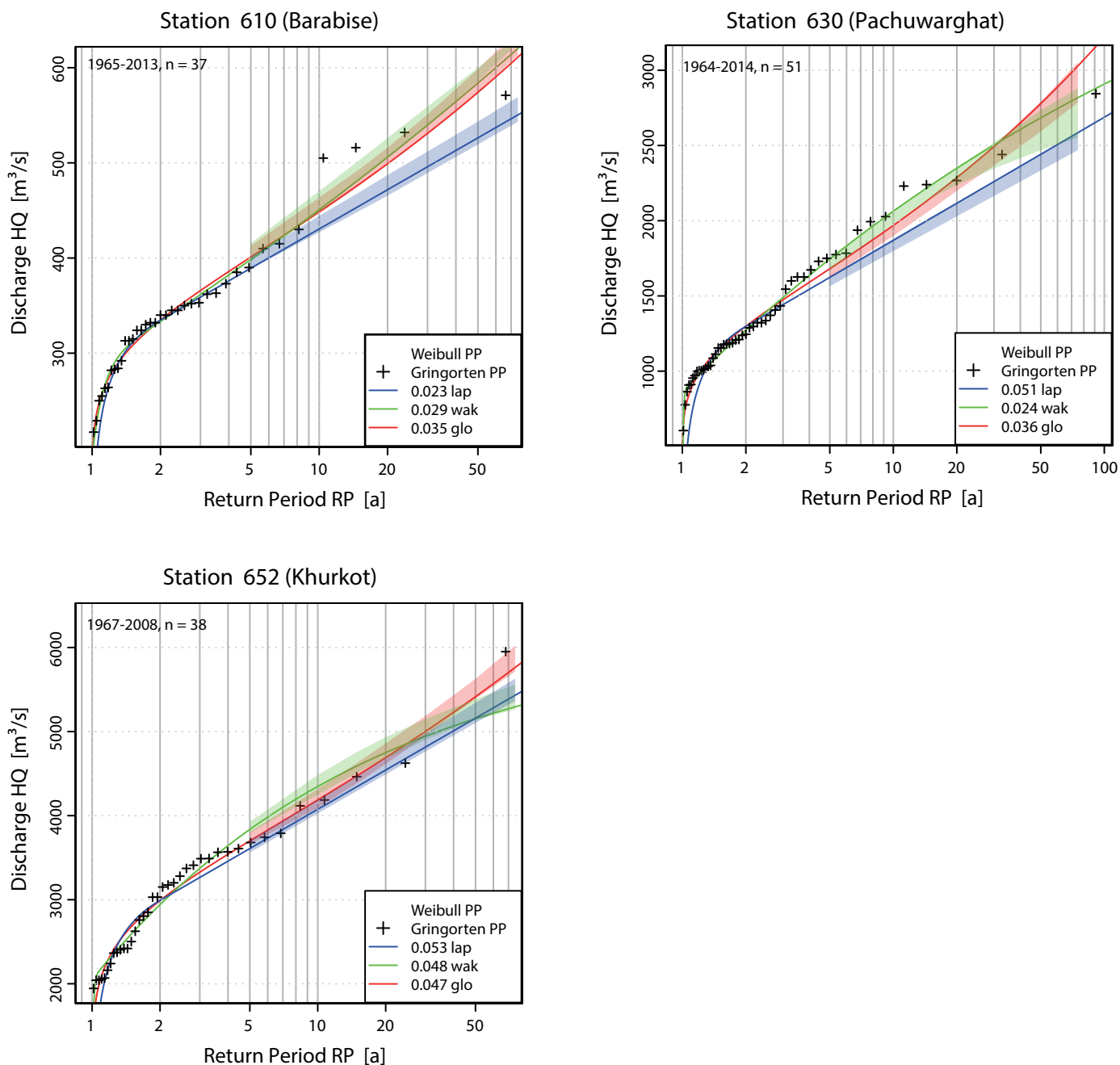
Fig. S11. Flood frequency analyses for four gauging stations along the Bhotekoshi/Sunkoshi River. Maximum yearly discharges were taken from records provided by the Nepal Department of Hydrology and Meteorology and by the Upper Bhotekoshi Hydropower project. The time span and number of years included for each record are indicated. Weibull PP and Gringorten PP are plotting positions of the real annual max discharge data following the distribution of Weibull or Gringorten. The return periods are fitted with three different distributions Lap = Laplace Distribution, Wak = Wakeby Distribution, Glo= Generalized Logistic Distribution. The choice to use these three out of 17 available is based on the three best fitting distributions for data from Barabise.
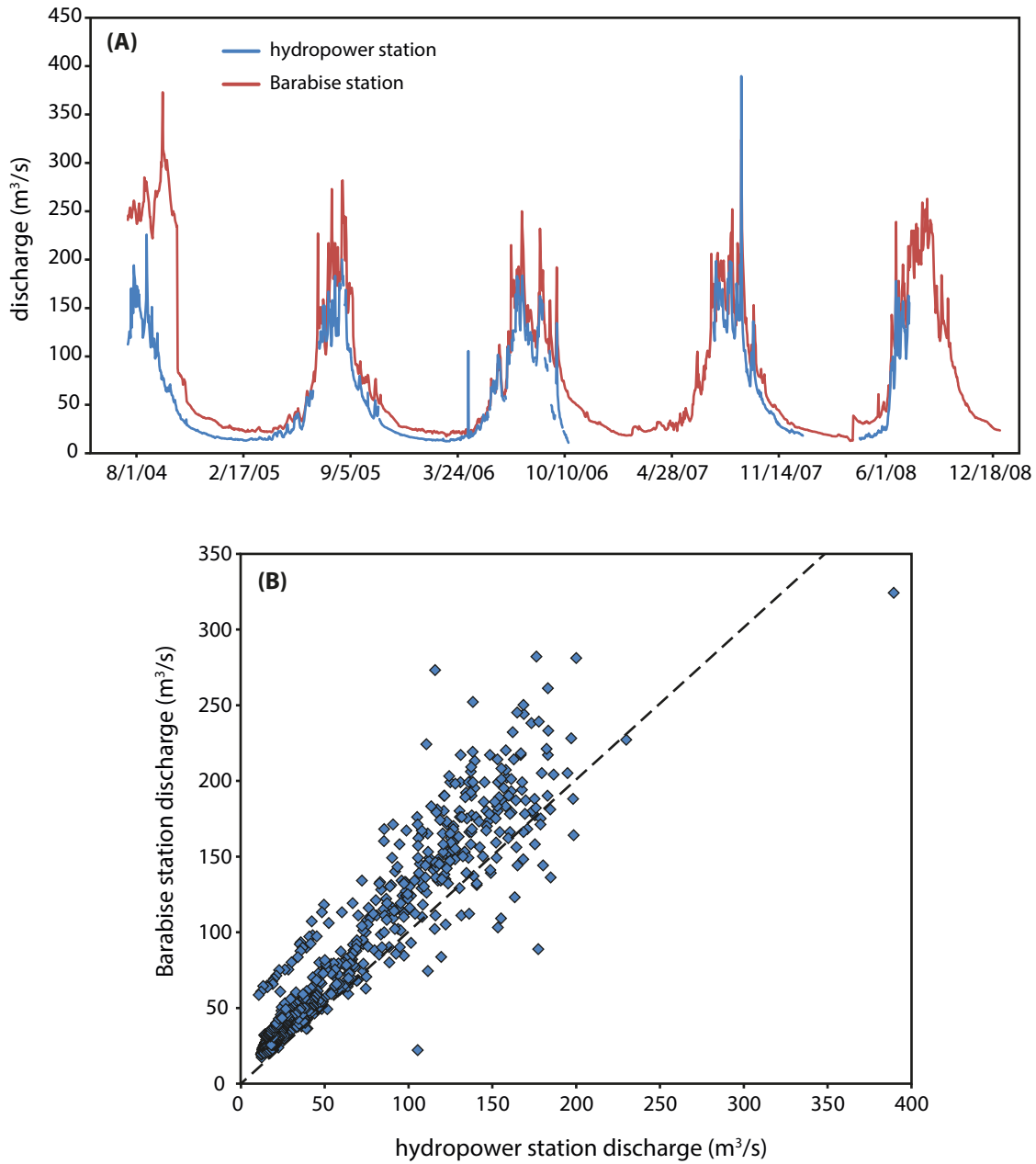
Fig. S12. Comparison of discharge at hydropower dam and Barabise. (A) time series of daily discharge measured at the hydropower dam and Barabise. Note that the summer/fall 2004 values at Barabise appear to have a problem, with an abrupt one-day drop in discharge on October 17. (B) daily discharge at the hydropower station plotted against discharge at Barabise, excluding 2004. Dashed line shows the 1:1 line.

Table S1

location	cross section area (m²)	perimeter (m)	hydraulic radius (m)	channel gradient	mean velocity (m/s)	manning's n	max depth (m)	discharge (m³/s)	+	-
Khukundol	292.95	68.13	4.30	0.024	8.19	0.05	6.0	2400	600	400
Chaku	259.66	63.33	4.17	0.025	6.82	0.06	5.3	1771	400	300
Borderlands resort	146.65	48.03	3.05	0.04	7.02	0.06	5.2	1155	300	100
Barabise	152.78	49.32	3.10	0.0085	4.9	0.04	4.8	749	200	100

Table S1. discharge calculations

Table S2

reach number	location	longitude	latitude	date first scans	date second scans	channel elevation change (m)	maximum bank erosion (m)	reach length (m)
1	Khukundol	85.934	27.924	04.03.2016	14.11.2016	-10	10	180
2	Hindi	85.920	27.908	03.03.2016	14.11.2016	-1	5-6	670
3	Listi road bridge	85.914	27.896	04.03.2016	15.11.2016	-2	4	345
4	upstream Chaku	85.913	27.889	11.10.2015	13.11.2016	-4	3-5	450
5	Chaku	85.910	27.884	10.10.2015	13.11.2016	-3	3-6	425
6	Chaku downstream	85.904	27.879	04.03.2016	15.11.2016	-1	5-9	1365
7	Kahole Khola	85.879	27.867	01.03.2016	12.11.2016	-0.3 to -1	2.5	500
8	Borderlands Resort	85.878	27.857	01.03.2016	12.11.2016	-0.5	2	285
9	Barabise	85.896	27.796	03.03.2016	16.11.2016	0-0.2	12-14	600

Table S2. Lidar survey summary

Table S3

tile	4551910	4552010	2552011
region	Barabise to border	border to to confluence	lake and Zhangzangbo River
image dates	31 October 2016	31 October 2016	29 October 2016
	01 October 2015	01 October 2015	01 October 2015
	28 May 2015*		
	11 October 2014	11 October 2014	
	06 November 2013	28 November 2013	
	12 March 2013	08 November 2012	
	11 October 2011	18 October 2011	
	25 October 2010	03 November 2009	

*only used for landslide mapping

Table S3. RapidEye imagary information

Table S4

location	latitude	longitude	30 yr flood discharge (m3/s)	upstream area (km^2)	distance (m)	distance (km)	1981 GLOF max discharge (m^3/s)	2016 GLOF max discharge (m^3/s)
Friendship bridge	27.973183	85.963946		1975	303780	86	6430	
Upper Bhotekoshi dam	27.938488	85.944547	< 550	2035	298811	91		
Phulpin bridge	27.930439	85.936520		2110	297631	92	4099	
Khukundol	27.920276	85.931132		2124	295297	94		2400
Chaku	27.882104	85.908563		2159	291079	99	2865	1771
Borderlands Resort	27.853777	85.877531		2291	285248	104		1030
bridge K94	27.837683	85.874904		2300	283070	107	2619	
Barabise 1	27.797471	85.895328	550	2362	275865	114	2316	750
Sunkoshi dam	27.757771	85.867512		2495	270129	120	1296	
Pachuwarghat	27.553746	85.749650	2500	4854	230419	159	768	
Khurkot	27.338350	85.993469	4990	10174	183248	206	1540	2000

Table S4. GLOF and 30 year discharge values

Table S5

channel parameters	value
mean grain roughness diameter (m)	0.25
mean transported bedload grain diameter (m)	0.1
standard deviation of grain diameter (based on log-raised cosine distribution) (dimensionless)	0.5
specific sediment density (kg / m^3)	2650
water flow depth (m)	varies from 3 to 6 m
flow width (m)	20
channel slope angle (radians)	0.025
distance from seismic station to source (m)	100, 900
ratio of bedload flux to transport capacity (dimensionless)	varies from 0.05 to 1
seismic parameters	
frequency range modeled (Hz)	(1,80)
reference frequency (Hz)	1
quality factor at f_0	20
phase speed of the Rayleigh wave at f_0 (m/s)	2175

Table S5. Parameters used to model frequancy spectra following *(15, 16)*

Table S6

Station 610 (Barabise)								
return period (years)	5	10	15	20	30	50	75
Laplace mean	394	436	461	478	503	534	558
Laplace 25th quantile	389	427	449	465	489	519	543
Laplace 75th quantile	401	444	469	487	512	543	569
Wakeby mean	405	459	492	515	549	593	629
Wakeby 25th quantile	396	448	482	504	539	586	625
Wakeby 75th quantile	416	470	503	526	559	600	633
Generalized Logistic mean	406	455	485	507	541	586	625
Generalized Logistic 25th quantile	400	447	476	499	531	575	613
Generalized Logistic 75th quantile	413	464	493	516	551	599	640

discharge (m³/s) — column label for Station 610

Station 630 (Pachuwarghat)								
return period (years)	5	10	15	20	30	50	75
Laplace mean	1600	1837	1975	2073	2212	2386	2525
Laplace 25th quantile	1564	1798	1933	2029	2164	2334	2469
Laplace 75th quantile	1632	1878	2024	2122	2264	2443	2586
Wakeby mean	1715	2012	2171	2277	2420	2587	2712
Wakeby 25th quantile	1672	1978	2146	2237	2347	2468	2552
Wakeby 75th quantile	1754	2071	2227	2353	2520	2734	2881
Generalized Logistic mean	1654	1927	2097	2224	2416	2679	2909
Generalized Logistic 25th quantile	1624	1898	2071	2199	2367	2593	2786
Generalized Logistic 75th quantile	1690	1971	2146	2285	2496	2792	3053

discharge (m³/s) — column label for Station 630

Station 652 (Khurkot)								
return period (years)	5	10	15	20	30	50	75
Laplace mean	3647	4118	4394	4590	4866	5214	5490
Laplace 25th quantile	3560	4025	4297	4490	4762	5103	5362
Laplace 75th quantile	3705	4185	4470	4681	4978	5342	5631
Wakeby mean	3872	4379	4626	4782	4979	5194	5342
Wakeby 25th quantile	3792	4251	4512	4682	4900	5139	5263
Wakeby 75th quantile	3927	4485	4760	4934	5149	5388	5560
Generalized Logistic mean	3735	4223	4515	4728	5041	5457	5809
Generalized Logistic 25th quantile	3660	4091	4389	4613	4946	5388	5713
Generalized Logistic 75th quantile	3807	4320	4630	4860	5185	5627	6024

discharge (m³/s) — column label for Station 652

Table S6. return period discharges

References and Notes

1. K. Hewitt, "Natural dams and outburst floods of the Karakoram Himalaya," in *Hydrological Aspects of Alpine and High-Mountain Areas*, J. W. Glen, Ed. (IAHS Publication No. 138, International Association of Hydrological Sciences, 1982), pp. 259–269.

2. P. K. Mool, Glacier lake outburst floods in Nepal. *J. Nepal Geol. Soc.* **11**, 273–280 (1995).

3. International Centre for Integrated Mountain Development (ICIMOD), "Glacial lakes and glacial lake outburst floods in Nepal" (ICIMOD, Kathmandu, 2011).

4. O. Korup, F. Tweed, Ice, moraine, and landslide dams in mountainous terrain. *Quat. Sci. Rev.* **26**, 3406–3422 (2007). doi:10.1016/j.quascirev.2007.10.012

5. J. E. Costa, R. L. Schuster, The formation and failure of natural dams. *Geol. Soc. Am. Bull.* **100**, 1054–1068 (1988). doi:10.1130/0016-7606(1988)100<1054:TFAFON>2.3.CO;2

6. M. J. Westoby, N. F. Glasser, J. Brasington, M. J. Hambrey, D. J. Quincey, J. M. Reynolds, Modelling outburst floods from moraine-dammed glacial lakes. *Earth Sci. Rev.* **134**, 137–159 (2014). doi:10.1016/j.earscirev.2014.03.009

7. D. A. Cenderelli, E. E. Wohl, Peak discharge estimates of glacial-lake outburst floods and "normal" climatic floods in the Mount Everest region, Nepal. *Geomorphology* **40**, 57–90 (2001). doi:10.1016/S0169-555X(01)00037-X

8. A. B. Shrestha, M. Eriksson, P. Mool, P. Ghimire, B. Mishra, N. R. Khanal, Glacial lake outburst flood risk assessment of Sun Koshi basin, Nepal. *Geomatics Nat. Hazards Risk* **1**, 157–169 (2010). doi:10.1080/19475701003668968

9. N. R. Khanal, J. M. Hu, P. Mool, Glacial lake outburst flood risk in the Poiqu/Bhote Koshi/Sun Koshi river basin in the Central Himalayas. *Mt. Res. Dev.* **35**, 351–364 (2015). doi:10.1659/MRD-JOURNAL-D-15-00009

10. W. Schwanghart, R. Worni, C. Huggel, M. Stoffel, O. Korup, Uncertainty in the Himalayan energy–water nexus: Estimating regional exposure to glacial lake outburst floods. *Environ. Res. Lett.* **11**, 074005 (2016). doi:10.1088/1748-9326/11/7/074005

11. D. Xu, Characteristics of debris flow caused by outburst of glacial lake in Boqu river, Xizang, China, 1981. *GeoJournal* **17**, 569–580 (1988). doi:10.1007/BF00209443

12. D. A. Cenderelli, E. E. Wohl, Flow hydraulics and geomorphic effects of glacial-lake outburst floods in the Mount Everest region, Nepal. *Earth Surf. Process. Landf.* **28**, 385–407 (2003). doi:10.1002/esp.448

13. D. Higaki, G. Sato, Erosion and sedimentation caused by glacial lake outburst floods in the Nepal and Bhutan Himalayas. *Glob. Environ. Res.* **16**, 71–76 (2012).

14. C. Huggel, A. Kääb, W. Haeberli, P. Teysseire, F. Paul, Remote sensing based assessment of hazards from glacier lake outbursts: A case study in the Swiss Alps. *Can. Geotech. J.* **39**, 316–330 (2002). doi:10.1139/t01-099

15. J. S. Kargel, G. J. Leonard, D. H. Shugar, U. K. Haritashya, A. Bevington, E. J. Fielding, K. Fujita, M. Geertsema, E. S. Miles, J. Steiner, E. Anderson, S. Bajracharya, G. W. Bawden, D. F. Breashears, A. Byers, B. Collins, M. R. Dhital, A. Donnellan, T. L. Evans, M. L. Geai, M. T. Glasscoe, D. Green, D. R. Gurung, R. Heijenk, A. Hilborn, K. Hudnut, C. Huyck, W. W. Immerzeel, J. Liming, R. Jibson, A. Kääb, N. R. Khanal, D. Kirschbaum, P. D. Kraaijenbrink, D. Lamsal, L. Shiyin, L. Mingyang, D.

McKinney, N. K. Nahirnick, N. Zhuotong, S. Ojha, J. Olsenholler, T. H. Painter, M. Pleasants, K. C. Pratima, Q. I. Yuan, B. H. Raup, D. Regmi, D. R. Rounce, A. Sakai, S. Donghui, J. M. Shea, A. B. Shrestha, A. Shukla, D. Stumm, M. van der Kooij, K. Voss, W. Xin, B. Weihs, D. Wolfe, W. Lizong, Y. Xiaojun, M. R. Yoder, N. Young, Geomorphic and geologic controls of geohazards induced by Nepal's 2015 Gorkha earthquake. *Science* **351**, aac8353 (2016). doi:10.1126/science.aac8353 Medline

16. K. Roback, M. K. Clark, A. J. West, D. Zekkos, G. Li, S. F. Gallen, D. Chamlagain, J. W. Godt, The size, distribution, and mobility of landslides caused by the 2015 M_w7.8 Gorkha earthquake, Nepal. *Geomorphology* **301**, 121–138 (2017). doi:10.1016/j.geomorph.2017.01.030

17. F. Gimbert, V. C. Tsai, M. P. Lamb, A physical model for seismic noise generation by turbulent flow in rivers. *J. Geophys. Res. Earth Surf.* **119**, 2209–2238 (2014). doi:10.1002/2014JF003201

18. V. C. Tsai, B. Minchew, M. P. Lamb, J. P. Ampuero, A physical model for seismic noise generation from sediment transport in rivers. *Geophys. Res. Lett.* **39**, L02404 (2012). doi:10.1029/2011GL050255

19. A. Burtin, L. Bollinger, J. Vergne, R. Cattin, J. L. Nábělek, Spectral analysis of seismic noise induced by rivers: A new tool to monitor spatiotemporal changes in stream hydrodynamics. *J. Geophys. Res. Solid Earth* **113**, B05301 (2008). doi:10.1029/2007JB005034

20. P. Chatanantavet, K. X. Whipple, M. A. Adams, M. P. Lamb, Experimental study on coarse grain saltation dynamics in bedrock channels. *J. Geophys. Res. Earth Surf.* **118**, 1161–1176 (2013). doi:10.1002/jgrf.20053

21. D. A. Cenderelli, B. L. Cluer, "Depositional processes and sediment supply in resistant-boundary channels: Examples from two case studies," in *Rivers Over Rock: Fluvial Processes in Bedrock Channels*, K. J. Tinkler, E. E. Wohl, Eds. (Geophysical Monograph Series, vol. 107, American Geophysical Union, Washington, DC, 1998), pp. 105–131.

22. A. C. Brayshaw, Bed microtopography and entrainment thresholds in gravel-bed rivers. *Geol. Soc. Am. Bull.* **96**, 218–223 (1985). doi:10.1130/0016-7606(1985)96<218:BMAETI>2.0.CO;2

23. Rastriya Samachar Samiti, "Heavy rain brings massive flood to Bhotekoshi River," *Himalyan Times*, 6 July 2016; https://thehimalayantimes.com/nepal/heavy-rain-brings-massive-flood-bhotekoshi-river.

24. J. D. Ives, R. B. Shrestha, P. K. Mool, "Formation of glacial lakes in the Hindu Kush-Himalayas and GLOF risk assessment" (ICIMOD, Kathmandu, 2010).

25. A. Lutz, W. W. Immerzeel, S. R. Bajracharya, M. Litt, A. Shrestha, "Impact of climate change on the cryosphere, hydrological regimes and glacial lakes of the Hindu Kush Himalayas: A review of current knowledge" (ICIMOD Research Report 2016/3, ICIMOD, Kathmandu, 2016).

26. D. R. Rounce, A. C. Byers, E. A. Byers, D. C. McKinney, Brief communication: Observations of a glacier outburst flood from Lhotse Glacier, Everest area, Nepal. *Cryosphere* **11**, 443–449 (2017). doi:10.5194/tc-11-443-2017

27. W. Schwanghart, A. Bernhardt, A. Stolle, P. Hoelzmann, B. R. Adhikari, C. Andermann, S. Tofelde, S. Merchel, G. Rugel, M. Fort, O. Korup, Repeated catastrophic valley

infill following medieval earthquakes in the Nepal Himalaya. *Science* **351**, 147–150 (2016). doi:10.1126/science.aac9865 Medline

28. J. D. Bricker, W. Schwanghart, B. R. Adhikari, S. Moriguchi, V. Roeber, S. Giri, Performance of models for flash flood warning and hazard assessment: The 2015 Kali Gandaki landslide dam breach in Nepal. *Mt. Res. Dev.* **37**, 5–15 (2017). doi:10.1659/MRD-JOURNAL-D-16-00043.1

29. S. G. Evans, J. J. Clague, Recent climatic change and catastrophic geomorphic processes in mountain environments. *Geomorphology* **10**, 107–128 (1994). doi:10.1016/0169-555X(94)90011-6

30. K. Hewitt, J. Liu, Ice-dammed lakes and outburst floods, Karakoram Himalaya: Historical perspectives on emerging threats. *Phys. Geogr.* **31**, 528–551 (2013).

31. S. R. Bajracharya, P. Mool, Glaciers, glacial lakes and glacial lake outburst floods in the Mount Everest region, Nepal. *Ann. Glaciol.* **50**, 81–86 (2009). doi:10.3189/172756410790595895

32. T. Bolch, A. Kulkarni, A. Kääb, C. Huggel, F. Paul, J. G. Cogley, H. Frey, J. S. Kargel, K. Fujita, M. Scheel, S. Bajracharya, M. Stoffel, The state and fate of Himalayan glaciers. *Science* **336**, 310–314 (2012). doi:10.1126/science.1215828 Medline

33. Y. Chen, C. Xu, Y. Chen, W. Li, J. Liu, Response of glacial-lake outburst floods to climate change in the Yarkant River basin on northern slope of Karakoram Mountains, China. *Quat. Int.* **226**, 75–81 (2010). doi:10.1016/j.quaint.2010.01.003

34. B. Schmandt, R. C. Aster, D. Scherler, V. C. Tsai, K. Karlstrom, Multiple fluvial processes detected by riverside seismic and infrasound monitoring of a controlled flood in the Grand Canyon. *Geophys. Res. Lett.* **40**, 4858–4863 (2013). doi:10.1002/grl.50953

35. B. Schmandt, D. Gaeuman, R. Stewart, S. M. Hansen, V. C. Tsai, J. Smith, Seismic array constraints on reach-scale bedload transport. *Geology* **45**, 299–302 (2017). doi:10.1130/G38639.1

36. D. L. Roth, N. J. Finnegan, E. E. Brodsky, D. Rickenmann, J. M. Turowski, A. Badoux, F. Gimbert, Bed load transport and boundary roughness changes as competing causes of hysteresis in the relationship between river discharge and seismic amplitude recorded near a steep mountain stream. *J. Geophys. Res. Earth Surf.* **122**, 1182–1200 (2017). doi:10.1002/2016JF004062

37. D. Lague, N. Brodu, J. Leroux, Accurate 3D comparison of complex topography with terrestrial laser scanner: Application to the Rangitikei canyon (NZ). *ISPRS J. Photogramm. Remote Sens.* **82**, 10–26 (2013). doi:10.1016/j.isprsjprs.2013.04.009

38. B. Boessenkool, extremeStat: Extreme Value Statistics and Quantile Estimation. R package version 1.3.0 (2017); https://CRAN.R-project.org/package=extremeStat.